Manuscript prepared for Atmos. Chem. Phys. Discuss.
with version 2.2 of the LaTeX class copernicus_discussions.cls.
Date: 24 January 2011

An aircraft case study of the spatial transition from closed to open mesoscale cellular convection over the Southeast Pacific

R. Wood[1], **C. S. Bretherton**[1], **D. Leon**[2], **A. D. Clarke**[3], **P. Zuidema**[4], **G. Allen**[5], **and H. Coe**[5]

[1]Atmospheric Sciences, University of Washington, Seattle, USA
[2]Atmospheric Science, University of Wyoming, Laramie, USA
[3]Department of Oceanography, University Hawai'i, Honolulu, USA
[4]Rosenstiel School of Marine and Atmospheric Science, University Miami, Miami, USA
[5]School of Earth, Atmospheric and Environmental Sciences, University Manchester, Manchester, UK

Correspondence to: R. Wood (robwood@atmos.washington.edu)

Abstract

Aircraft measurements are presented from 27 to 28 October 2008 case study of the VOCALS Regional Experiment (REx) over the remote subtropical southeast Pacific (18° S, 80° W). Data from two aircraft that took measurements approximately twelve hours apart but in the same advected airmass are used to document a remarkably sharp spatial transition in marine boundary layer (MBL), cloud, and aerosol structure across the boundary between a well-mixed MBL containing overcast closed mesoscale cellular stratocumulus, and a pocket of open cells (POC) with significantly lower cloud cover. Long ($\sim$190–250 km) straight and level flight legs at three levels in the marine boundary layer and one level in the lower free troposphere permit sampling of the closed cells, the POC, and a 20–30 km wide transition zone with distinctly different structure from the two airmasses on either side. The POC region consists of intermittent active and strongly precipitating cumulus clouds rising and detraining into patches of drizzling but quiescent stratiform cloud which is optically thin especially toward its edges.

Mean cloud-base precipitation rates inside the POC are several mm d^{-1}, but rates in the closed cell region are not greatly lower than this. This latter finding suggests that precipitation is not a sufficient condition for POC formation from overcast stratocumulus. Despite similar cloud-base precipitation rates in the POC and overcast region, much of the precipitation ($>$90%) evaporates below cloud in the overcast region, while there is significant surface precipitation inside the POC. In the POC and transition region, although the majority of the condensate is in the form of drizzle, the integrated liquid water path is remarkably close to that expected for a moist adiabatic parcel rising from cloud base to top.

The transition zone between the POC and the closed cells often consists of thick "boundary cell" clouds producing mean surface precipitation rates of 10–20 mm d^{-1}, a divergent quasi-permanent cold/moist pool below cloud, a convergent inflow region at mid-levels in the MBL, and a divergent outflow near the top of the MBL.

The stratiform clouds in the POC exist within an ultra-clean layer that is some 200–300 m thick. Aerosol concentrations (N_{a}) measured by a PCASP in the diameter range 0.12–3.12 µm in the center of the ultra-clean layer are as low as 0.1–1 cm^{-3}. This suggests that coalescence

scavenging and sedimentation is extremely efficient, since $N_{\rm a}$ in the subcloud layer, and droplet concentration $N_{\rm d}$ in the active cumuli are typically 20–60 cm^{-3}. The droplet concentrations in the quiescent stratiform clouds are extremely low (typically 1–10 cm^{-3}), and most of their liquid water is in the form of drizzle, which mainly evaporates before reaching the surface. The cloud droplet concentration in the overcast region decreases strongly as the transition region is approached, as do subcloud accumulation mode aerosol concentrations, suggesting that coalescence scavenging is impacting regions in the overcast region as well as inside the POC. Both flights show lower accumulation mode aerosol concentration in the subcloud layer of the POC ($N_{\rm a}\sim$30 cm^{-3}) compared with the overcast region ($N_{\rm a}\sim$100 cm^{-3}), but elevated (and mostly volatile) total aerosol concentrations are observed in the POC at all levels around 20–50 km from the transition zone, perhaps associated with some prior nucleation event. Despite the large differences in cloud and MBL structure across the POC-overcast boundary, the MBL depth is almost the same in the two regions, and increases in concert over the 12 h period between the flights.

1 Introduction

The influence of the structure, dynamics, and microphysics of marine stratocumulus clouds on the nature and quantity of the precipitation that they produce has been a focus of research stretching back over seventy years to pioneering studies by Walter Findeisen in the late 1930s which showed that even relatively thin, low liquid water content clouds could produce drizzle-sized drops through collision-coalescence (see Mason, 1957). Simpson (1941) and Squires (1952) discuss observer reports of precipitation falling from warm clouds in the subtropics and tropics. Mason (1952) showed theoretically that clouds thinner than 1 km can produce drizzle that can reach the surface especially if the cloud is turbulent. The aircraft observations of Mason and Howorth (1952) and Singleton (1960) demonstrated unequivocally that warm stratocumulus clouds as thin as 300–600 m can produce surface drizzle.

Squires (1958a,b) opened up the study of factors controlling warm rain formation including the importance of increased cloud droplet concentration, and hence aerosol concentration, for

reducing the propensity for precipitation formation in low cloud. Very little work then followed until interest in stratocumulus clouds grew and a significant number of aircraft case studies of marine stratocumulus showed drizzle to be a common feature (Brost et al., 1982; Nicholls, 1984; Nicholls and Leighton, 1986; Austin et al., 1995; Bretherton et al., 1995) and, importantly, that precipitation rates were frequently sufficient enough to play an important role in the cloud moisture budget. Sensitive millimeter radar studies also began to shed light on the structure of precipitation in marine low cloud (Frisch et al., 1995; Miller and Albrecht, 1995; Vali et al., 1998) and were central in establishing that drizzle is intermittent and can be locally strong, particularly where cumulus clouds are growing and detraining into a marine stratocumulus layer above.

Together, these aircraft and radar studies engendered the idea that stratocumulus precipitation might exert an influence on the stability of the boundary layer, and thus cloud dynamics and structure. This notion fuelled various modeling studies of varying complexity (e.g., Liou and Ou, 1989; Albrecht, 1989; Wang et al., 1993; Feingold et al., 1997; Stevens et al., 1998; Savic-Jovcic and Stevens, 2008) which all showed sensitivity of cloud cover, thickness, and MBL structure to drizzle. Many of these modeling studies suggest that drizzle, particularly if it is strong (cloud base precipitation rates on the order of $1\,\mathrm{mm\,d^{-1}}$), has a tendency to decrease cloud cover because drizzle acts to stabilize the MBL by suppressing moisture transport into the cloud and promoting decoupling. Recent radar and satellite observations have revealed a striking connection between the mesoscale morphology of marine stratocumulus and the degree to which they precipitate, with spatial transitions between regions of closed and open mesoscale cellular convection frequently associated with an increase in precipitation strength (Bretherton et al., 2004; Stevens et al., 2005; Comstock et al., 2005, 2007). It is thus reasonable to suppose that drizzle plays a significant role in setting the climatological cloud cover. However, since there have been only very limited aircraft missions contrasting precipitation and cloud structure transitions between open and closed cells (Van Zanten and Stevens, 2005; Sharon et al., 2006), there are many remaining questions regarding the way in which precipitation impacts MBL cloud coverage and thickness.

Cloud modeling studies have advanced the assertion (Squires, 1958a,b) that increased cloud

droplet concentration could limit precipitation and have opened a pathway through which increasing atmospheric aerosols might alter cloud cover regionally (Liou and Ou, 1989; Albrecht, 1989). Studies collating many aircraft and remote sensing measurements have confirmed the hypothesis that stratocumulus drizzle rates are sensitive to cloud droplet concentration (Pawlowska and Brenguier, 2003; Comstock et al., 2004; Van Zanten et al., 2005; Wood, 2005; Geoffroy et al., 2008). Without adequate controls, it has proven difficult to establish observationally whether microphysically-suppressed precipitation is able to increase stratocumulus cloud cover or thickness. Cloud resolving model studies suggest that increased cloud condensation nucleus (CCN) concentrations can induce non-monotonic responses in cloud cover (Xue et al., 2008) and cloud thickness (Ackerman et al., 2004). These responses are the result of competing effects with increased CCN suppressing precipitation formation but, as a consequence, increasing the lateral and cloud-top entrainment that tends to reduce cloud volume (Wood, 2007; Xue et al., 2008; Stevens and Feingold, 2009).

Ship and aircraft observations show large reductions in CCN concentration, and consequently lower cloud droplet concentration, within pockets of open cells (POCs) embedded in overcast marine stratocumulus (Sharon et al., 2006; Van Zanten and Stevens, 2005; Wood et al., 2008). Spaceborne remote sensing measurements of cloud droplet effective radius are consistent with such microphysical contrasts (Stevens et al., 2005; Rosenfeld et al., 2006; Wood et al., 2008), and there is a tendency for regions of open cells to be embedded within overcast cloud regions with low cloud droplet concentrations (Wood et al., 2008). This, together with the finding that open cells forming within marine subtropical stratocumulus are rarely found close to the coasts (Wood and Hartmann, 2006), may tempt one to attribute the formation of POCs to low CCN concentrations since low CCN would drive stronger precipitation all else being equal. Cloud resolving model simulations do indeed show that spatial CCN gradients can induce precipitation gradients that lead to closed/open cell cloud morphology gradients (Wang and Feingold, 2009). The conclusion that CCN differentials are the primary trigger of POCs in nature, however, may be difficult to establish since we also know from simple calculations that mean precipitation rates within POC regions ($\sim$1 mm d^{-1}) are sufficient to drive significant rates of depletion of CCN through coalescence scavenging (Wood, 2006). For a 1 km deep boundary layer the

timescale for CCN removal through coalescence scavenging is only $\sim$1.5 d for a cloud base precipitation rate of 1 mm d^{-1} (Wood, 2006). Therefore, we would expect precipitation differentials, which might be driven by dynamics, to drive CCN differentials. The tight coupling between microphysics and dynamics within POCs, and perhaps within drizzling stratocumulus boundary layers in general is therefore an intriguing area where improved measurements may shed important light on POC formation mechanisms.

Here, we present aircraft measurements from two aircraft flights sampling the same broad region of transition between overcast stratocumulus and a pocket of open cells, taken over an 18 h period (27/28 October 2008) during the VOCALS Regional Experiment (REx)[1]. A major focus of VOCALS-REx is an improved understanding aerosol-cloud-precipitation interactions within drizzling stratocumulus clouds and the role that these interactions play in driving mesoscale cloud variability. As such, the aircraft missions documented here are the first dedicated specifically to documenting the transitions between an overcast region of closed mesoscale cells and a pocket of open cells embedded within it.

This paper describes observations from an aircraft case study contrasting the structure and dynamics of the spatial transition from overcast marine stratocumulus to a pocket of open cells. The organization of the paper is as follows. Section 2 describes the sampling, instrumentation, and data. Section 3 describes the mesoscale structure and the rationale for breakdown into different regions, while Sect. 4 describes the large scale context. The mean structure and the cloud/aerosol microphysics are presented in Sects. 5 and 6, respectively. Section 7 is a discussion and introduces a conceptual model of the transition from overcast to open cells. Conclusions are drawn in Sect. 8.

[1]The VOCALS (Variability of the American Monsoon Systems Ocean-Cloud-Atmosphere-Land Study) Regional Experiment (VOCALS-REx) is an international field program designed to make observations of poorly understood but critical components of the coupled climate system of the southeast subtropical Pacific, a region dominated by strong coastal upwelling, extensive cold SSTs, and home to the largest subtropical stratocumulus deck on Earth. Further details of the program can be found at http://www.eol.ucar.edu/projects/vocals/

2 Data and methodology

2.1 Flight and leg details

Data from two research flights are used in this study. Table 1 details the flight legs from the Facility for Airborne Atmospheric Measurements BAe-146 flight B409 on 27 October 2008, and the NSF C-130 flight RF06 on 28 October 2008.

Figure 1 shows visible satellite imagery of the sampled POC and environs approximately 3 h after the end of the C-130 measurements. As seen in the GOES whole-disk image (Fig. 1), an extensive sheet of stratocumulus is present over the Southeast Pacific in the Arica Bight area off the coast of Northern Chile/Southern Peru, and it is punctuated by a large region of open cells which extends westwards of 79° W, as seen in the MODIS image (Fig. 1, top panel). The sampled POC is an eastward extension of this broader region of open cells. Figure 2 shows an GOES infrared sequence for a 44 h period encompassing the two flights. The evolution of a narrow, quasi-linear POC feature into a broad expanse of open cells is clearly shown. Despite considerable diurnal variability in the clouds near the coast and in the far SW of the region shown in Fig. 2, in the region of the POC feature itself there is no clear evidence of diurnal variability. There are two key points that make it difficult to determine diurnal variability in this case: (a) high clouds are masking our ability to clearly delineate from satellite the evolution overnight on the 27/28 October; (b) aircraft sampling issues including their location with respect to the POC-overcast boundary make it difficult to separate diurnal variability from evolution of the POC feature independent of diurnal variability.

Flight B409 was conducted during the late afternoon hours of 27 October with science sampling from 21:40 to 22:50 UTC (16:40–17:50 LT). The flight consisted of three straight and level legs. Trajectories estimated using NCEP GFS analysis and short-range forecast fields were used to position the C-130 in the same airmass as that sampled by the BAe-146 during B409 roughly 12 h earlier. Flight RF06 was conducted during the early morning hours of 28 October with the science sampling taking place from 08:00 to 13:30 UTC (03:00–08:30 LT). The flight consisted of a series of six straight and level legs 190–250 km in length which were designed to sample the transition between a POC and the surrounding overcast closed cellular stratocumulus. In

addition, a sawtooth run with the aircraft climbing and descending from 100 m above the inversion to approximately 100 m below stratocumulus cloud base was carried out, and profiles were taken well into the POC and overcast regions. All runs and profiles are oriented NNE-SSW with headings of 30/210°, which resulted in approximately Lagrangian airmass sampling over 5.5 h. At the end of the legs, 180° turns of opposite handedness (left then right then left, etc.) were used, which led to a slight upstream lateral drift of the legs with respect to the mean flow ($\sim$60 km over the 5.5 h). This ensured that the sampling of the boundary, which as Fig. 1 shows is quite heterogeneous on the $<$100 km scale, was not biased by repeatedly sampling the same set of cells throughout the flight.

Figures 3 and 4 show sections of the BAe-146 and C-130 flight tracks overlaid on near-coincident GOES IR and (when sufficient sunlight permits) visible imagery, during missions B409 and RF06, respectively. Patches of thin high cloud are evident on both flights, particularly in the IR, and preclude good spaceborne visualization of the boundary especially in the hours before sunrise (10:42 UTC) on RF06. Both flights sample the boundary between a pocket of open cells to the SW and overcast stratocumulus to the NE, although the cloud layer straight and level run in B409 appears to skim the eastward edge of the POC feature. On both flights, the boundary between the open and closed cells is rather uneven and consists of cellular cloud features with horizontal scales of 20–40 km. As the gray dashed line in Fig. 4 shows, the boundary between the open and closed cell regions appeared to be advecting with the mean wind in the MBL during the course of flight RF06.

2.2 Instrumentation

Full details of the instrumentation flown on the C-130 and BAe-146 during VOCALS-REx are given in Wood and coauthors (2011). We present data from numerous instruments including atmospheric state variables and winds (standard C-130 or BAe-146 instruments), cloud liquid water content (Particle Volume Monitor, PVM on the C-130 and Johnson-Williams/Nevzorov on the BAe-146), drizzle liquid water content and drop size distribution ($r>30$ µm, 2-D-C optical array probe), and cloud droplet concentration $N_{\rm d}$ and size distribution ($1<r<23.5$ µm, Droplet Measurement Technologies Cloud Droplet Probe, CDP). All measurements were ana-

lyzed at 1 Hz time resolution unless otherwise stated. The 2-D-C probe flown on the C-130 in VOCALS was modified by doubling the number of diodes from 32 on the conventional probe to 64. The electronics were updated which reduces the number of particles lost due to slow signal ramping. Counts from the first two size bins were excluded since the sample volume for these particles is difficult to determine. The 2-D-C thus sampled drops with radii larger than approximately 30 µm.

Size distributions of dry particles measured on the C-130 are reported at 60 s resolution by merging cabin-sampled size distributions from the following instruments: a custom build radial differential mobility analyzer (RDMA, dry diameters 10–150 nm), a "long" DMA (LDMA, diameters 10–500 nm), a custom modified PMS LAS-X optical particle counter (OPC, diameters 150–1000 nm) and a TSI model 3321 aerodynamic particle sizer (APS, diameters 0.78–10 µm). Details are given in Clarke et al. (2007). In addition, an externally-mounted PCASP gives nominally dry size distributions for diameters 120–3000 nm. Total aerosol concentrations N_{CN} are measured with TSI 3025 and 3010 CN counters ($>$3 nm and $>$10 nm, respectively). Aerosol size distributions on the BAe-146 are measured using an SMPS system with total concentrations from a TSI CN counter. On the C-130 one of the inlets to the 3010 CN counters is heated to $\sim$350 °C which is sufficient to volatilize sulfuric acid and ammonium/sulfate salts and provide the concentration $N_{\mathrm{CN,hot}}$ of non-volatile CN (these measurements are described in Clarke et al., 2007). From this we estimate the volatile fraction $f_{\text{non-ref}}$ of total particles larger than 10 nm.

The C-130 flew a substantial remote sensing suite during VOCALS. Measurements used in this study are upwelling and downwelling broadband fluxes (from solar and IR pyranometers), profiles of radar reflectivity Z from the zenith and nadir-viewing 95 GHz University of Wyoming Cloud Radar (WCR), lidar backscatter profiles from the zenith-viewing Wyoming Cloud Lidar (WCL), and microwave radiances from a wing-mounted zenith-viewing 183 GHz G-band microwave radiometer (GVR).

2.3 Derived data products

Several derived data products are used in this study. Data at 1 Hz time resolution (100 m horizontal resolution) from the WCR on the C-130 are used to derive (a) cloud top height $z_{\rm top}$ for those clouds with significant radar echoes, using a threshold of -35 dBZ; (b) column maximum radar reflectivity $Z_{\rm max}$; (c) near-surface reflectivity $Z_{\rm sfc}$. Precipitation rates are estimated from $Z_{\rm max}$ and $Z_{\rm sfc}$ using Z–R relationships appropriate for drizzling stratocumulus (Comstock et al., 2004). From the maximum reflectivity we derive the column maximum precipitation rate $R_{\rm max}{=}(Z_{\rm max}/25)^{0.77}$ and from the near-surface (250 m) reflectivity Z_{250} we derive a 250 m precipitation rate $R_{250}{=}(Z_{250}/57)^{0.91}$. In addition, the in-situ drop size distribution measurements from the 2-D-C probe are used to estimate the precipitation rate assuming terminal velocities from Pruppacher and Klett (1997).

Cloud top height is taken to be the highest gate where the WCR return is determined to reflect scattering from hydrometeors rather than receiver noise or other artifacts. To avoid spurious cloud top height determinations caused by random variations and non-ideal behavior of the receiver noise, a combination of thresholds is used for each range gate: over half of the samples within the 1 s average must exceed the standard deviation of the noise and the 1 s average must exceed 1.5 times the standard deviation of the noise; the variance of the Doppler velocities within the second must be less than 0.4 time the variance associated with noise; finally, cloud top height must be within $\pm$100 m of the median cloud top height for the leg.

The C-130 WCL lidar backscatter profile is used to determine the cloud base altitude using a maximum gradient method. Cloud cover is also determined from subcloud legs using the WCL by identifying cloud features above the aircraft.

Liquid water path (LWP) is derived from the GVR on the C-130 using the 183.31$\pm$14 GHz channel as described in (Zuidema and coauthors, 2010). Such estimates are only available for the two subcloud legs (Table 1).

2.4 Distinguishing cloudy, clear, and drizzling samples

Each 1 Hz data sample is classified as being either cloudy, clear, or containing drizzle (but not cloudy) using a combination of sensors. To be classified as cloudy, either the PVM or CDP liquid water mixing ratio has to exceed $0.03\,\mathrm{g\,kg^{-1}}$. To be classified as containing drizzle, the sample must not be cloudy as defined above, but the 2-D-C probe must indicate a drizzle drop concentration of at least $1\,\mathrm{L^{-1}}$. All samples not classified as cloudy or drizzle-containing are deemed to be clear.

In this paper, we refer to the PVM-measured liquid water as the *cloud* liquid water mixing-ratio q_{L} since the PVM instrument is relatively insensitive to droplets with radii greater than approximately 25 µm (Wendisch et al., 2002). Since the 2-D-C counts drops with radii larger than 30 µm, there is little overlap between the PVM and the 2-D-C, and so we refer to the 2-D-C measured liquid water as the *drizzle* liquid water mixing ratio q_{D} in this study.

3 Mesoscale structure

3.1 Delineation of POC, overcast and transition regions

Figure 5 shows radar reflectivity from the straight and level and sawtooth legs in RF06 as a function of distance along the run. A zone of strong echoes was frequently present in the transition zone between the overcast stratocumulus and the more broken cloud associated with the POC. This region of strong precipitation represents the transition zone between overcast and POC, and we term the mesoscale cloud structure associated with this the *boundary cell*. The POC-ward extent of the boundary cell we term the *leading edge* and the location where the overcast stratocumulus clouds begin we refer to as the *back edge*. The leading edge was diagnosed subjectively based upon the WCR imagery. The images in Fig. 5 are aligned so that the leading edge is defined as being zero distance. The location of a back edge is harder to define since for four of the runs the boundary cell is not all that clearly separated from the echoes associated with the overcast stratocumulus (e.g. runs SC1, CB, SC2, C2). For other legs

(AC, C1 and S), there is a clear gap between the strongly precipitating echo and the overcast stratocumulus. Figure 5 denotes the location of the back edge by a vertical dashed line. We refer to the region between the leading and back edge as the *transition region* separating the POC from the overcast stratocumulus. The width of the transition region ranges from 16 to 43 km (see also Table 1). The location of the transition region moved roughly consistently with the mean wind in the MBL on RF06, and the edge observed with the satellite although a conclusive assessment of this is not possible with the flight strategy used.

The key features contrasting similarities and differences in the MBL, cloud, precipitation and aerosol structure between the POC and overcast regions are summarized in Table 2. The following sections of the paper constitute a presentation of the observational data upon which this summary is based.

3.2 Overcast region

Since the column maximum reflectivity $Z_{\max}$ is typically found near the cloud base (Comstock et al., 2004), $Z_{\max}$ is a good indicator of the precipitation rate near cloud base R_{CB}. Almost all of the overcast region can be characterized by columns with maximum reflectivity $Z_{\max}$ greater than -20 dBZ (Fig. 5). Remarkably, 92% of columns in the overcast region sampled by the WCR have $Z_{\max}{>}-15$ dBZ (Fig. 6), which is the threshold commonly assumed for the presence of significant drizzle (-15 dBZ corresponds to roughly 0.1 mm d^{-1} precipitation rate according to Comstock et al., 2004). For roughly a quarter of all columns in the overcast region $Z_{\max}{>}0$ dBZ, corresponding to cloud base precipitation rates R_{CB} of $\sim$2 mm d^{-1} (see upper axis in Fig. 6), and 2% of the columns have $Z_{\max}$ as high as 10 dBZ. It is clear, therefore, that the overcast stratocumulus clouds surrounding the POC are producing substantial drizzle.

Figure 5 also shows that the precipitation within the overcast region is not uniform but is organized into cellular structures containing core regions with high $Z_{\max}$ surrounded by regions with much lower $Z_{\max}$. This cellularity in marine stratocumulus is consistent with the closed mesoscale cells seen in the satellite imagery (Fig. 1), which have a dominant horizontal scale of some 30–40 km, a typical value for stratocumulus over the Southeast Pacific (Wood and Hartmann, 2006).

3.3 POC region

The POC region is characterized by lower cloud cover and the POC clouds are organized into open cells (e.g., Fig. 1). Approximately 55–60% of the POC columns sampled contain reflectivities exceeding -28 dBZ (Fig. 6). The more sensitive WCL detected clouds 60% of the time from subcloud runs in the POC indicating that most clouds in the POC contained reflectivities large enough to be detected by the radar. As in the overcast region, roughly a quarter of the POC has $Z_{\max}>0$ dBZ ($R_{\mathrm{CB}}>2\,\mathrm{mm\,d^{-1}}$) but the occurrence of heavy drizzle ($Z_{\max}>10$ dBZ) is three times more likely inside the POC than in the surrounding overcast regions. There are also relatively fewer incidences of weak precipitation ($-20<Z_{\max}<-10$ dBZ) inside the POC. Thus, there is a fundamentally different nature to the precipitation inside the POC compared with the surrounding overcast clouds, with a broader distribution of $Z_{\max}$ and locally stronger precipitation.

3.4 Transition region

The distribution of $Z_{\max}$ within the transition region is shifted to higher $Z_{\max}$ values than in the POC and overcast regions (Fig. 6). Around 65% of the transition region has $Z_{\max}>0$ dBZ, 30% has $Z_{\max}>10$ dBZ ($R_{\mathrm{CB}}>10\,\mathrm{mm\,d^{-1}}$), and roughly 5% has $Z_{\max}>20$ dBZ ($R_{\mathrm{CB}}>70\,\mathrm{mm\,d^{-1}}$), which emphasizes that the drizzle in the transition region can be locally very heavy indeed. The distribution of $Z_{\max}$ is not as broad as in the POC region, being closer to the distribution in the overcast region except shifted to higher reflectivities. Inspection of Fig. 5 confirms that the strongest precipitation in most flight legs is associated with boundary cells that are frequently present in the transition region.

4 Large scale context

Tables 3 for flight B409 and 4 for flight RF06 show a number of key large scale variables, some of which are estimated separately for the POC and overcast regions, which constitute the meteorological forcings on the MBL. During the earlier flight B409 the MBL was advecting in

approximately SSE flow which becomes more southeasterly by the time of RF06. The wind speed increases slightly from 7.5 m s^{-1} to 9 m s^{-1} between the flights. The sea-surface temperature (SST) is slightly warmer than the air temperature. The near-surface air temperature inside the POC is cooler than in the overcast region (by 0.3 K on B409 and 0.9 K on RF06), and some of this difference can be explained by cooler SSTs in the POC (see Table 4). Surface estimated sensible heat fluxes (SHF) are small ($<$15 W m^{-2}) throughout. However, the estimated latent heat flux (LHF), however, is large (115–130 W m^{-2} on B409 increasing to 122 W m^{-2} in the POC and 160 W m^{-2} in the overcast on RF06). This contributes an additional 8-12 W m^{-2} to add to the SHF, giving surface virtual heat fluxes of 20-25 W m^{-2} which is not an insubstantial surface contribution to buoyant production.

The primary driver of turbulence in the MBL is the longwave radiative flux divergence across the MBL, which averages 91 W m^{-2} in the overcast stratocumulus in RF06 (Table 4), a particularly high value due to low values of downwelling flux ($F\downarrow$) above the MBL caused by the very dry free-troposphere ($q$$<$1 g kg^{-1} on both B409 and RF06). Despite the visual impression of a lack of cloud in the POC region (e.g., Fig. 1), the actual cloud cover is $\sim$60% (Sect. 3.3 above) on RF06 leading to 72 W m^{-2} of radiative flux divergence across the MBL in the POC region. However, much of the extensive cloud in the POC consists significantly lower liquid water path (see Sect. 5.3 below), and contains very large droplets. Therefore the optical thickness and emissivity of the extensive POC clouds will be lower than that in the overcast region, so that longwave radiative flux divergence will be distributed over a thicker layer and may therefore be less effective at driving buoyant circulations in the POC. This behavior has been found in large-eddy simulation studies for clouds with similar characteristics to those in the POC studied here (Ackerman et al., 1993).

The most marked difference between the two flights is the MBL depth which increases from 1280 m on B409 to 1375 m on RF06, with uncertainties in these estimates being some 30 m determined from inter-profile variability. The MBL is capped with a very strong inversion throughout. The difference in potential temperature between 200 m above the inversion and the inversion base is $\sim$12–13 K in the POC and $\sim$15 K in the overcast regions (Tables 4 and 3). Visually, the cloud top in the overcast region was quite flat. From the various inversion-crossings,

no significant difference in MBL depth was detected between the overcast and POC regions on either flight. In both regions the mean cloud top height is located close to the inversion base, but there are some clouds in the POC whose tops are up to 150 m below the inversion base, in agreement with the DYCOMS-II RF02 case study of Petters et al. (2006).

The MBL is under the influence of large scale divergence, at least in the daily mean (Table 4). It is interesting that this is the case despite negative dv/dy (the strongly positive du/dx is double the magnitude of the negative dv/dy). Since the POC boundary is aligned approximately WNW/ESE (Fig. 4), this significant deformation to the flow implies a stretching component along the direction of the POC boundary and a convergent flow toward the boundary.

5 Mean structure

5.1 Conserved variables

Profiles of liquid potential temperature (θ_l) and total water content (q_t, the sum of the vapor (dewpoint hygrometer), cloud liquid (PVM/CDP), and drizzle liquid (2-DC/2-DS) water mixing ratios) from both leg-mean data and representative individual profiles are shown in Fig. 7. On both flights the overcast region MBL is remarkably well-mixed given the significant drizzle that the clouds are producing. The remarkably strong inversion ($\sim$15 K inversion jump in θ_l) is clearly evident. The inversion jump in the POC region is closer to $\sim$12 K, in the mean, although the RF06 POC profile happens to be through a cumulus cell and so is warmer than the mean conditions.

In the mean, on RF06 the POC region is more strongly stratified than the overcast region (Fig. 7), both in θ_l and in q_t, and the transition region even more so, with strong cold/moist pooling of air near the surface. Liquid potential temperature in the upper MBL in the POC exceeds that in the overcast region by 1.5 K, but is colder by roughly the same amount near the surface. The mean total water content in the upper MBL is greater in the overcast region by some 0.3–0.6 g kg^{-1}, but near the surface, the POC is moister than the overcast region by close to 1 g kg^{-1}. The POC region sampled on B409 is actually slightly drier than the overcast region

(Fig. 7) Approximately two thirds of the way up the MBL $\theta_{\rm l}$ and $q_{\rm t}$ are roughly the same in the overcast and POC. It is interesting that the MBL mean value of $\theta_{\rm l}$ is slightly lower and $q_{\rm t}$ slightly higher inside the POC than outside. This would be consistent with weaker entrainment inside the POC than outside, although differences in radiative heating or surface fluxes over the airmass history preclude definitive attribution. Data taken on flight B409 12 h prior to the RF06 measurements show a very similar structure with a well-mixed boundary layer and very similar mean values of $\theta_{\rm l}$ and $q_{\rm t}$ (Table 3 and Fig. 7), but with an inversion base that is approximately 100 m lower than that observed during RF06. The latter finding is consistent with entrainment deepening of the MBL over the period between the two flights (see Sect. 7 below).

Tracers that have higher concentrations in the free-troposphere than in the MBL (e.g. carbon monoxide (CO) and ozone) are less abundant in the POC MBL than in the overcast MBL. For example, on RF06 the CO concentration is 0.5–2 ppb lower inside the POC, and the ozone concentration 2–4 ppb lower. Similar overcast/POC differences in CO (1.8 ppb) and ozone (1.6 ppb) are found for the subcloud layer leg on flight B409, implying longevity in the horizontal gradients and structure across the POC-overcast boundary. Since the dry deposition rate of CO is small, and the free-tropospheric values measured in RF06 were approximately equal above the POC and the overcast regions, the observed MBL differences could represent integrated differences in entrainment rate. However, since we do not know either the history of the air entrained into the MBL prior to RF06, or the concentrations in the MBL before the POC formed, this cannot be concluded with certainty. The same is the case for ozone, which has the added complication of significant dry deposition and short timescale photochemical sources/sinks.

5.2 Condensate and drizzle on RF06

Profiles of cloud ($q_{\rm L}$) and drizzle ($q_{\rm D}$) liquid water mixing ratio from the straight and level runs on RF06 are shown in Fig. 8, and profiles of precipitation rate (2-D-C plus radar-estimated), relative humidity, drizzle drop size and number are shown in Fig. 9. In the cloud layer of the overcast region, $q_{\rm L}$ significantly exceeds $q_{\rm D}$, $q_{\rm L}$ increases upward, and $q_{\rm D}$ downwards in the cloud. This is typical behavior for overcast drizzling stratocumulus (Wood, 2005). By 300–400 m below cloud base, little drizzle water remains in the overcast region. Since the cloudbase

precipitation rates (Fig. 9a) in the overcast region are substantial at 2–4 mm d^{-1}, this indicates strong evaporation in the layer immediately below cloud base.

In the POC and transition regions, as inferred from cloud-level flight legs, $q_{\rm D}>q_{\rm L}$ (Fig. 8) indicating that the majority of the condensate is present as precipitation rather than cloud water. Averaged over the two cloud layer legs, the ratio $q_{\rm D}/q_{\rm L}$ is approximately 3 in the POC region and 4 in the transition region (in contrast with the overcast region where it is only 0.25). Therefore, a marked transition from cloud to drizzle condensate appears to be a signature of the transition from closed to open cellular convection. The mean total condensate mixing ratio in the cloud layer of the POC region is significantly lower than that in the overcast region when weighted by the fraction of samples that are cloudy (35% of POC samples from the two cloud legs are cloudy, in contrast to 92% of those in the overcast region), but the in-cloud means are approximately equal.

The transition region observed on RF06 contains the heaviest precipitation (Fig. 9a), where mean values are 10–20 mm d^{-1} at all levels. In this region there is also a substantial quantity of drizzle liquid water present close to the surface (Fig. 8b), with somewhat less in the POC and almost none in the the overcast region. This largely reflects the lower cloud base and high relative humidity (Fig. 9b) both of which hinder drizzle evaporation. Interestingly, the drizzle drop volume radius $r_{\rm v,D}$ is largely independent of region but is a strong function of height (Fig. 9c), so that the mean size of the drizzle drops leaving cloud base increases from the overcast ($\sim$80 µm) to POC ($\sim$100 µm) to transition ($\sim$140 µm) region. The strong height scaling of $r_{\rm v,D}$ independent of region suggests that the mean size of drizzle drops is largely a function of the depth of cloud that produces them rather than other factors. One consequence of this is that since the depth of the layer that a drizzle drop can fall before evaporating scales strongly with $r_{\rm v,D}$ (Comstock et al., 2004), it is not surprising that the fraction of the cloudbase precipitation rate reaching the surface increases strongly from the overcast ($<$10% reaching surface) to the POC ($\sim$25% reaching surface), and is higher still in the transition region where most of the drizzle reaches the surface (Fig. 9a).

A striking feature, observed with both in-situ and radar data, is that the mean precipitation rate at the cloud level in the overcast region is significant (3–4 mm d^{-1}) and about three quar-

ters of that in the POC (4–5 mm d^{-1}). Thus, the thinking that POCs delineate regions in marine stratocumulus with locally enhanced precipitation (Stevens et al., 2005) may need to be revised. Examination of MODIS-retrieved liquid water path (Fig. 10) from 4 h after RF06 shows that the POC feature sampled is itself embedded in a broader swath of thick overcast stratocumulus with peak values of liquid water path at the center of the mesoscale cells exceeding 400 g m^{-2} and a mean LWP of 150–200 g m^{-2}. Our observations from RF06 are indicating that this surrounding cloud contains significant cloud base precipitation. Since elevated LWP is known to be associated with enhanced precipitation in marine stratocumulus (Comstock et al., 2004; Wood, 2005; Kubar et al., 2009, and see also Sect. 5.4 below) it seems reasonable to conclude that the high LWP swath, rather than simply the POC, may delineate regions of locally enhanced precipitation and that this broad region of precipitation supports the formation of the POC. This is consistent with existing satellite analysis over the southeast Pacific (Wood et al., 2008) showing that open cellular convection is positively correlated with elevated LWP in overcast clouds surrounding the open cells.

Since $r_{\mathrm{v,D}}$ is similar in all regions at a given height, variations in precipitation rate at a given height level are more strongly reflective of variations in the drizzle drop concentration N_{D} (Fig. 9d). This is consistent with previous aircraft observations (e.g., Van Zanten et al., 2005) and with observed exponents relatively close to unity in the relationship between reflectivity and rain rate (Comstock et al., 2004).

5.3 Cloud vertical structure on RF06

Figure 11a indicates striking differences in the cloud LWP distributions in the POC, overcast, and transition regions. The cloud LWP distribution in the overcast region is narrow with a mode at 200 g m^{-2}, a slight positive skewness, a mean of 240 g m^{-2}, and only a few instances where LWP exceeds 500 g m^{-2}. The POC LWP distribution has a mode at close to zero, a mean of 210 g m^{-2}, and is broader and more positively skewed, with some 15% of POC clouds with LWP exceeding 500 g m^{-2}. The transition region has the largest mean LWP (510 g m^{-2}) with a broad distribution and little skewness.

Cloud top height z_{top} is well-sampled with the cloud radar and is shown in Fig. 11b. Narrow

distributions characterize the overcast and the transition regions, where the standard deviation of $z_{\rm top}$ is approximately 40 m. In the POC the distribution is somewhat broader (standard deviation closer to 50 m) and there is evidence of bimodality, consistent with photographic information (not shown). Interestingly, the means of the distributions in each of the three regions are within 15 m of each other (1345 m in the POC to 1360 m in the overcast), but the highest and lowest cloud tops are found in the POC. Further investigation shows that the highest cloud tops in the POC are those with the largest values of the column maximum reflectivity $Z_{\rm max}$, and thus are the most strongly precipitating cells.

Cloud base height $z_{\rm cb}$ distributions (Fig. 11c) are much broader than those in cloud top in all three regions. This result is in accordance with previous studies of mesoscale variations of overcast stratocumulus (Wood and Taylor, 2001). The narrowest distribution is in the overcast region. In the POC region there is a bimodal distribution of $z_{\rm cb}$, with the lowest bases corresponding to cumuli which grow from the top of the surface mixed layer, and the highest bases consistent with stratocumulus and thin stratus aloft. The cloud base height in the transition region is unimodal and somewhat higher than the cumulus bases in the POC.

Further insight into the vertical structure of the clouds in the MBL across the POC-overcast boundary is provided in Fig. 12 which shows zenith-viewing radar and lidar backscatter for the entirety of the subcloud run SC2, together with liquid water path observations from the microwave radiometer. Radar-derived cloud top height and maximum radar reflectivity are overlaid on the lidar backscatter which indicates a remarkable degree of agreement between the height of the cloud base $z_{\rm b}$ (delineated by strong lidar backscatter in regions with moderate or no drizzle) and the height of the maximum radar reflectivity $z_{\rm Zmax}$. The coincidence of the $z_{\rm b}$ and $z_{\rm Zmax}$ is to be expected because drizzle drops grow by collection monotonically downward in the cloud but begin to evaporate as soon as they fall into the subsaturated region below cloud base (Comstock et al., 2004; Wood, 2005), but the agreement is striking nonetheless. Further, this agreement suggests that $z_{\rm Zmax}$ may be used instead of a lidar-derived $z_{\rm b}$ in cases where the drizzle is sufficiently heavy to cause substantial lidar backscatter thus making it difficult to objectively determine a cloud base (for example, throughout much of the transition region in Fig. 12).

Figure 12 further exemplifies the narrow distribution of LWP in the overcast region, the high values in the transition region, and the intermittent distribution in the POC. What is particularly interesting is that in all regions and for all observed values of LWP, the clouds appear to be well-modeled with an adiabatic assumption. This is true whether the model uses the lidar-derived or, in strong drizzle, the maximum radar reflectivity-derived cloud base height. That even very strongly drizzling clouds, in which much of the condensate is in the form of drizzle (Fig. 8), retain an adiabatic liquid water path presumably indicates that the replenishment time for liquid water path through cloud updrafts is sufficiently strong to overcome the loss of liquid water to precipitation (see e.g., the simple adiabaticity model in Wood, 2005). In addition, the vertical motions may also prevent loss to drizzle by keeping drizzle drops lofted, thus hindering fallout. However, since there are substantial lateral mesoscale motions, regions of high liquid water content could be advected into regions with elevated cloud base, leading to superadiabatic liquid water contents as deduced from a one-dimensional perspective.

5.4 Factors controlling precipitation

The clouds with the strongest radar echoes correspond to those with the greatest liquid water path (Fig. 12), emphasizing the key role that the liquid water path plays in driving precipitation formation in these clouds.

Figure 13 builds on this by showing the relationship between cloud liquid water path (LWP) and the median column-maximum radar reflectivity $Z_{\max}$ for clouds in the POC, overcast, and transition regions. In general, the strongest precipitation is associated with the clouds with the highest LWP, which the analysis of the previous section indicates are the thickest clouds. This result is not particularly surprising in the light of previous measurements indicating that LWP/cloud thickness is a strong driver of precipitation in marine stratocumulus (see review by Brenguier and Wood, 2009). What is interesting is that in the POC and transition regions the relationship between LWP and $Z_{\max}$ diverges from that in the overcast, but that the divergence only occurs for LWP values lower than $\sim$400 g m^{-2}. This indicates that for $Z_{\max}$ greater than 5 dBZ (equivalent to a cloud base precipitation rate of a few mm d^{-1}), the precipitation rate appears to be explained primarily by LWP. There is little evidence that the significant differences

in N_{d} (see Sect. 6) between POC and overcast regions have any bearing on the ability of the thicker clouds (400 g m^{-2} adiabatic LWP is equivalent to a 600 m thick cloud) to precipitate. On the other hand, lighter precipitation rates typical of thinner clouds cannot be explained by variability in LWP alone, which leaves open a role for the lower N_{d} values in the POC to play a role in enhancing the precipitation efficiency compared with the overcast clouds. These results are broadly consistent with satellite observations, large eddy, and heuristic drizzle models (Feingold and Siebert, 2009; Kubar et al., 2009; Wood et al., 2009b; Sorooshian et al., 2009).

6 Cloud microphysics and aerosols

There are striking cloud microphysical and aerosol differences between the POC and the overcast regions that are as dramatic as those in the cloud and precipitation macrostructure. Table 5 provides cloud droplet concentrations, cloud droplet effective radii, and mean clear-air aerosol for selected levels in the POC, the transition region, and the overcast region on flight RF06.

6.1 Cloud droplet concentration and effective radius

Mean cloud droplet concentration N_{d} for clouds in the cloud layer of the overcast region is approximately 70 cm^{-3}, while in the POC it is an order of magnitude lower. Similar gradients were observed on the B409 flight 12 h earlier, implying that the microphysical gradients can be maintained over significant periods of time. This is a remarkable contrast, and results in strong differences in the cloud effective radii r_{e}. If drizzle drops are included in the r_{e} estimates (Table 5) the differences are even more striking. While drizzle drops can contribute significantly to r_{e} (Wood, 2000), the magnitude of the contribution in the POC and the transition regions is a doubling of r_{e} (Table 5). Figure 14 shows the MODIS-derived r_{e} near cloud top, showing values of 12–25 µm in the overcast region to the north of the POC where the aircraft sampled overcast clouds roughly 4 h earlier. These values are somewhat larger than those measured on the cloud legs in the overcast region, but it must be borne in mind that the cloud legs were quite close to the base of the cloud and that in well-mixed overcast stratocumulus clouds, the

effective radius increases with height (e.g., Martin et al., 1994). Given the cloud top and base heights in the overcast region, and since the impact of drizzle near cloud top is relatively small (Wood, 2005), we estimate that the cloud top effective radius should be roughly 30–40% greater than that for the cloud droplets at the height of the cloud legs, i.e. 13–14.5 µm or so. This is somewhat lower than the mean MODIS-derived value in the overcast region (17 µm), consistent with previous comparisons (e.g., Nakajima et al., 1991). In the POC region MODIS retrievals are not performed in most cases and so comparison with in-situ data is not meaningful.

6.2 Aerosol size distributions and concentrations

Aerosol size distributions for different heights in the POC and overcast regions from RF06 using the in-cabin University of Hawaii system are shown in Fig. 15. Both individual and mean spectra are shown to give a sense of the variability of the distribution. Aerosol distributions from B409 and RF06 in the subcloud region of the POC and overcast regions are shown in Fig. 16 and indicate dramatic differences in the aerosol properties between the two regions. We describe particular characteristics of the two primary submicron modes in the following subsections.

6.2.1 Accumulation mode particles

In the subcloud layer, the concentration $N_{\rm a}$ of particles with diameters 0.12–3.12 µm (measured with the PCASP during RF06) is three times higher in the overcast region ($N_{\rm a}{\sim}90\,{\rm cm}^{-3}$) than in the POC region ($N_{\rm a}{\sim}30\,{\rm cm}^{-3}$), where the concentrations are among the lowest values measured anywhere in the clean MBL (Table 5). The size distributions confirm this strong reduction in accumulation mode aerosol in the subcloud layer of the POC (Fig. 15d,e). A remarkably similar contrast between the accumulation mode of the aerosol distribution in the POC and the overcast regions is also observed on flight B409 approximately 12 h earlier (Fig. 16). Droplet concentrations in the more active cumuli in the POC are in the range 20–30 ${\rm cm}^{-3}$ (see Sect. 6.4 below), which is consistent with the subcloud PCASP concentrations. Likewise, the mean $N_{\rm d}$ values in the overcast region are similar to the mean subcloud $N_{\rm a}$ there. Low values of $N_{\rm a}$ in the POC are consistent with measurements made during the passage of a rift of open cells

encountered in a ship cruise to the same region (Tomlinson et al., 2007; Wood et al., 2008). The subcloud POC $N_{\rm a}$ is somewhat consistent with the aerosol distribution found in the DYCOMS RF02 POC study (Ackerman et al., 2009) which had an accumulation mode peaking at d=0.12 µm (so only half of it would be measured by a PCASP) and a modal concentration of 65 cm^{-3}.

It is interesting that although there are considerably lower accumulation mode aerosol concentrations in the POC subcloud layer, the lidar returns from these aerosols are significantly stronger (by a factor of 2 or 3) than those in the overcast region (see Fig. 20a). This may reflect the higher relative humidity there (Figs. 9b and 20c), but may also reflect changes in the concentration of supermicron sized particles. Given that near-surface wind speed inside and outside the POC are almost identical (Table 4), the surface source would be expected to be quite similar. However, the decoupled nature of the POC region may mean that the surface-produced (mainly supermicron) particles are mixed over a shallower depth than in the overcast, more well-mixed region. This issue warrants further exploration in future studies.

It is interesting that despite considerable coalescence scavenging that would be expected from the drizzle rates observed in the overcast region, the concentrations of aerosols and the size distribution measured in the overcast region subcloud layer on B409 and RF06 are very similar, indicating little time change in CCN between flights. Based on the analysis of Wood (2006), and drizzle rates observed on the flights, we would expect coalescence scavenging to remove $\sim$50 cm^{-3} CCN over a 12 h period. That we do not see decreases of this magnitude indicates that CCN must be being replenished, either through a surface source or by entrainment from the free-troposphere. Our estimates of entrainment rate (see Sect. 7 below) together with the concentrations of potential CCN in the FT (which are substantially lower on B409 than on RF06, not shown), indicate that entrainment likely provides an insufficient supply, and that a significant surface CCN source may be necessary.

Above the subcloud layer, while $N_{\rm a}$ stays roughly constant in the overcast region (i.e. determined on the CB leg below cloud) consistent with the well-mixed nature of the MBL there, $N_{\rm a}$ drops dramatically with height in the POC, reaching minimum values roughly 125–275 m below the inversion base (roughly 1100–1250 m altitude) of less than 1 cm^{-3} (Table 5 and Fig. 15c).

Data from seven separate profiles within the POC region all show minima in $N_{\rm a}$ in the range 0.1–1 $\rm cm^{-3}$. Leg mean values from the C1/C2 legs (at altitudes of 1157 and 1084 m, slightly below the minima in $N_{\rm a}$) in the POC have mean values of 2 $\rm cm^{-3}$ (Table 5). Figure 17 shows aerosol concentrations for different size classes from a representative profile in the POC region, which highlights the ultra-clean layer that exists within and near the top of the cumulus-coupled layer. Within the ultra-clean layer there has been a near-complete removal of the accumulation mode. Since concentrations in the lower free-troposphere are substantially higher than those anywhere in the POC MBL, entrainment cannot account for the low $N_{\rm a}$ in the ultra-clean layer, and so it is reasonable to conclude that the aerosols that would have been transported from the subcloud layer and detrained into this layer by cumulus have been almost completely scavenged and removed by precipitation. Indeed, the low mean $N_{\rm a}$ in the ultra-clean layer implies that entrainment is a particularly inefficient process in the POC for buffering MBL aerosols with FT aerosols. In the overcast region, however, the MBL is more well-mixed, with $N_{\rm a}$ in the FT lower than that in the MBL. However, the total aerosol concentrations in the free-troposphere exceed those in the MBL, and the size distributions (Fig. 15b,e) are consistent with a free-tropospheric source of new particles that then grow by aqueous phase processing.

6.2.2 Small aerosol particles

Total aerosol concentrations $N_{\rm CN}$ (Table 5) in the subcloud layer of the POC in RF06 are marginally greater ($N_{\rm CN}$=150 $\rm cm^{-3}$) than those in the overcast region ($N_{\rm CN}$=140 $\rm cm^{-3}$), which implies that the concentration of Aitken mode particles inside the POC ($\sim$120 $\rm cm^{-3}$) is almost three times the concentration of such particles outside the POC. This is clearly shown as a mode at $\sim$20 nm diameter in the size distributions (Fig. 15d,e). The dominant contribution of the Aitken mode to the total aerosol concentration in the POC was noted in the DYCOMS-II RF02 study (Petters et al., 2006), in which the suggestion was made that there may be a source of new particles inside the POC that is not present in the overcast. Alternatively, there may be a sink of small particles in the overcast region that is not occurring in the POC. That there is a distinct mode and not a monotonically increasing concentration with decreasing size indicates that any new particle formation is not taking place at the time of either the B409 or RF06 mea-

surements, and may have occurred some time earlier. Concentrations in the 20 nm mode were significantly higher in the POC 12 h earlier (compare B409 and RF06 spectra in Fig. 16), but the mode shapes are very similar. This is consistent with the removal of the 20 nm mode over time by Brownian coagulation on cloud droplets, perhaps following a daytime nucleation event prior to B409. Figure 15a,b shows that it is unlikely, although not impossible, that the free-troposphere could be a significant source of the small particles, since the concentrations there are typically smaller than those in the subcloud layer in the POC. Data from the B409 flight, where concentrations of aerosols in the FT were particularly low (not shown), also suggest that the FT is an unlikely source for the 20 nm mode particles in the POC.

The dominant sinks of small particles are Brownian diffusion onto existing particles or coalescence scavenging (Wood, 2006). Because there is a good relationship between the droplet concentration in updrafts and the subcloud PCASP concentration (not shown) it appears that the population of particles smaller than the PCASP range largely remains unactivated. It is thus likely that coalescence scavenging is a relatively unimportant sink of sub-PCASP sized particles in either region. Brownian diffusion losses on the larger overall surface area in the overcast region depends extremely strongly upon the size of the small particles. Aerosols with radii of 20 nm and greater have Brownian scavenging efficiencies that are much lower than those of freshly nucleated aerosol (Seinfeld and Pandis, 1996), but it is not possible to entirely rule out Brownian scavenging by cloud droplets as a cause for removal of the small particles. Brownian scavenging would certainly be a stronger sink in the overcast region where the total available cloud droplet surface area is significantly greater than that in the POC.

Additional evidence regarding the reasons for the larger CN concentration inside the POC can be found in the volatile fraction of total CN, estimated as $f_{\text{non-ref}}=(N_{\text{CN}}-N_{\text{CN,hot}})/N_{\text{CN}}$ (Table 5). Values of $f_{\text{non-ref}}$ in the POC are 0.5–0.7, much greater than the 0.25–0.3 found in the overcast. Since the CN concentrations in the layers below cloud in the POC and overcast are similar, this means that there is a substantially greater number of volatile particles in the POC than outside the POC. It seems to be difficult to account for these differences as a result of either particle losses or entrainment, and so we hypothesize that the enhanced CN in the POC are a result of new particle formation in the POC. Since the ultrafine (3–10 nm) concentrations

in the POC were not strongly elevated, it is suggested that the particles formed during the previous day, with precursor build up perhaps requiring photochemically-produced oxidants which may have been subsequently depleted by deposition onto the new particles. Elevated CN concentrations were found during a POC passage measured during a ship cruise to the same region (Wood et al., 2008), suggesting that this case is not unique, and evidence of new particle formation and size growth from the same passage was also presented in Tomlinson et al. (2007).

It is puzzling why the mode at 20 nm diameter is more dominant in the subcloud run than in the cloud layer (Fig. 15), since one would expect stronger nucleation to have occurred in the ultraclean layer where aerosol surface area is very low. However, if these particles were nucleated hours earlier, a stronger sink from coagulation onto cloud droplets may have depleted concentrations there. There is also considerable variability in the concentrations around 20 nm in the subcloud layer (Fig. 15d), so uncertainties associated with sampling a highly heterogeneous field must be borne in mind. We note that locally high CN concentrations ($\sim$300 cm^{-3}) are actually observed in the POC on the C1 leg even though the mean value in this layer (Table 5) is considerably lower. Since precipitation events are highly intermittent, the scavenging would also be expected to be patchy.

6.3 Variability of cloud and aerosol microphysics

Figure 18 shows time series of PCASP aerosol concentration ($N_{\rm a}$, clear samples) and cloud droplet concentration ($N_{\rm d}$, cloudy samples) plotted as a function of the distance from the leading edge of the transition region on flight RF06. This highlights the remarkable variability in the POC, particularly above the subcloud layer, and contrasts with the more homogeneous overcast region. These series are consistent with the variability in the aerosol size distributions (Figs. 15 and 16). In the POC, $N_{\rm d}$ ranges from 0.1 cm^{-3} to approximately 50 cm^{-3}, with the highest values in active cumulus updrafts, and (although to a lesser extent) in the compensating downdrafts of the cumuli (Fig. 19), and the lowest values in air with near-zero vertical motion. Note that in the upper MBL in the POC, there is strong variability even outside the active updrafts which is consistent with oscillations in the vertical extent of the ultra-clean layer possibly driven by gravity waves (see also Fig. 17.

The active cumuli in the POC are often quite broad (few km) in horizontal extent and essentially constitute the brightest clouds that form the open cell boundaries evident in the visible imagery (Figs. 1 and 14). Droplet concentrations in the most active cumuli of the POC greatly exceed the PCASP concentrations in the clear regions of the upper MBL in the POC, but are similar to the *subcloud layer* PCASP aerosol concentrations (Fig. 18 and Table 5). This result confirms that the subcloud layer represents the source of the air in the cumuli in the POC. The subcloud layer PCASP concentrations are much more homogeneous in space than those in the upper two-thirds of the MBL ($>$500 m), which indicates that the upper MBL air that is strongly depleted of aerosols mixes down to the subcloud layer very slowly. This seems consistent with recent large eddy simulations (Jonker et al., 2008) which show that most of the compensating downward motion in cumulus fields is not in the form of slow subsidence in the clear regions between clouds, but is confined primarily to relatively strong but localized downdrafts close to the cumuli. Since we observe relatively high $N_{\rm d}$ values in the strong compensating cumulus downdrafts (Fig. 19), this suggests that the extremely low mean values of $N_{\rm a}$ (and $N_{\rm d}$) in the ultra-clean layer may be less closely linked to the active cumuli than one might suppose given the strong association of much of the POC precipitation with the active cumuli (Fig. 19b). Perhaps there is another loss mechanism involving the widespread and quiescent clouds, including the thin stratus, that does not depend upon coalescence scavenging in the strongly-precipitating cumuli. This might be a slow and steady but widespread sedimentation of large cloud and small drizzle drops in the quiescent clouds that results in the formation of the ultra-clean layer near the top of the MBL in the POC.

Another interesting feature seen in Fig. 18 is the dramatic decline in $N_{\rm d}$ which begins in earnest approximately 20–30 km from the transition region. At the back edge of the transition region $N_{\rm d}$ is only a few drops cm^{-3} even though the subcloud layer $N_{\rm a}$ in this region does not fall below about 30 cm^{-3} (although $N_{\rm a}$ does show a decrease towards the transition region). The low $N_{\rm d}$ may indicate signficant coalescence scavenging by drizzle in this region. This region of decreasing $N_{\rm d}$ is also one in which CO concentrations drop from values typical of the overcast region to values typical of the POC (not shown). This suggests that, in the overcast region, as the transition is approached, more and more air from the POC is present at the cloud

level. One hypothesis is that this region comprises air detrained from the boundary cell, which is itself a mixture of subcloud air from the POC and the overcast regions. Model simulations should shed considerably more light on the mesoscale dynamics, but these are beyond the scope of this study.

Figure 20a shows remarkable variability in the lidar backscatter due to aerosols in the POC, with very little scattering above the subcloud layer, and considerable variability within it, with curiously strong returns in the POC region immediately adjacent (e.g. -20 to 0 km from the leading edge) to the boundary cell, and very weak returns on the overcast side (e.g. 25–35 km from the leading edge). On SC1 at least, $N_{\rm a}$ is actually higher here than on overcast side of the boundary cell (Fig. 18), consistent with the aerosol scattering differences being driven not only by relative humidity differences but by significant changes in aerosol concentrations.

7 Turbulence and entrainment rate estimates combining the two flights

Using the 12 h time difference between B409 and the middle of the sampling on RF06, we estimate the mean entrainment rate using three different budgets: (a) mass; (b) energy; (c) moisture. The basic approach for this is outlined in Caldwell et al. (2005), but here we apply it to the budgets between the two flights. We choose to estimate a single entrainment rate for the POC and overcast regions together. The mass budget uses the observed increase in MBL depth between B409 and RF06, together with the subsidence rate (Table 4), to estimate the rate at which the MBL must have entrained over the 12 h period between the two flights. The MBL depth was found to increase from 1285 m to 1375 m over this period, and the subsidence rate over this period is estimated to be 0.1–0.2 cm s^{-1} (note that the value given in Table 4 is a diurnal mean), resulting in an entrainment rate of $w_{\rm e}$=0.3–0.5 cm s^{-1}. The chief source of error is in the subsidence rate which has a significant diurnal cycle in the SEP region that is still not fully understood (Wood et al., 2009a).

The energy budget requires assessment of the infrared radiative flux divergence over the MBL, the surface precipitation rate, and the surface sensible heat flux, for which we use the measurements in RF06 since there was more extensive sampling. From Table 4 the LW flux

divergence is $-78\,\mathrm{W\,m^{-2}}$ and the sensible heat flux is $12\,\mathrm{W\,m^{-2}}$. We estimate that the mean surface precipitation rate is approximately $1\,\mathrm{mm\,d^{-1}}$, or $28\,\mathrm{W\,m^{-2}}$ in energy terms. The storage term is estimated to be slightly negative ($-5\,\mathrm{W\,m^{-2}}$). The jump in liquid potential temperature across the inversion is approximately 12 K. The largest source of error is likely to be the surface precipitation rate estimate, and the storage term, which combined may result in an uncertainty in the entrainment rate of a factor of two, i.e. w_e=0.2–0.4 $\mathrm{cm\,s^{-1}}$.

The water budget requires estimates of the surface precipitation rate, the latent heat flux at the surface. As with the energy budget the moisture storage term was found to be close to zero. From Table 4 the latent heat flux is some $140\,\mathrm{W\,m^{-2}}$, and the jump in total water across the inversion approximately $7.5\,\mathrm{g\,kg^{-1}}$, from which we estimate w_e=0.45–0.7 $\mathrm{cm\,s^{-1}}$, with the largest source of uncertainty being the storage term ($0.5\,\mathrm{g\,kg^{-1}}$ uncertainty in the MBL mean temperature change between flights leads to a 40% change in the derived w_e.

Given the three estimates and their uncertainties, our best estimate of the mean entrainment rate for the POC, overcast and transition regions between the two flights is $0.45\pm0.1\,\mathrm{cm\,s^{-1}}$. This is consistent with mean nighttime entrainment rates of 0.4–0.6 $\mathrm{cm\,s^{-1}}$ estimated from the EPIC Stratocumulus Cruise in 2001 (Caldwell et al., 2005), and suggests that the POC-overcast boundary region is actively entraining despite the strong cloudbase drizzle rates. These estimates should prove useful for testing model simulations of the POC/overcast boundary. In general, modeling studies give conflicting information on the degree to which strong drizzle suppresses entrainment in stratocumulus, with Stevens et al. (1998) suggesting a marked impact, consistent with theoretical ideas for mixed layers (Wood, 2007), while the more recent intercomparison of large eddy models by Ackerman et al. (2009) finds that drizzle does not have a marked effect on entrainment.

Since there are no significant differences in the MBL depth between the POC and overcast regions on either of the flights, this implies either that the entrainment in the POC is the same as that in the overcast region, or that there is a different subsidence rate in the POC and the overcast regions. The vertical wind variance measured in the overcast cloud layer is almost double that in the POC ($0.60\,\mathrm{m^2s^{-2}}$ in the overcast vs. $0.32\,\mathrm{m^2s^{-2}}$ in the POC on RF06), although sampling limitations in the highly variable POC region must place significant error on these variance

estimates. The mean inversion strength is only 10–20% greater in the overcast region. To the extent that the vertical wind variance difference are real, since cloud top entrainment rates in stratocumulus scale with the ratio of the the wind variance and the inversion strength, we would expect that the stronger turbulence in the overcast region would lead to substantially stronger entrainment there. That this does not result in a more rapidly growing MBL in the overcast region suggests that the subsidence rate is weaker in the POC region than in the overcast region. This is unlikely to be caused by the large scale divergence which would be expected to vary only weakly in space, and so it suggests that there may be a compensating circulation between the overcast and POC regions which effectively "holds-up" the MBL in the POC despite weaker entrainment. Model simulations of this case (Bretherton et al., 2010; Berner and Bretherton, 2010) do indeed show differences in entrainment rate across the boundary and yet an inversion that rises in concert.

8 Discussion and conceptual model

A conceptual diagram of the POC-transition-overcast boundary layer is shown in Fig. 21. In-situ and radar doppler wind data (Fig. 23) indicate significant mid-level inflow ($\pm 2\,\mathrm{m\,s^{-1}}$) into the boundary cells in the transition region, consistent with the typical behavior observed in strongly precipitating stratocumulus cells in the southeast Pacific (Comstock et al., 2007). Outflow is observed in radar winds at the cloud level which then detrains air into the surrounding POC and overcast regions. Evaporation of strong precipitation with rates of 10–20 $\mathrm{mm\,d^{-1}}$ below cloud-base appears to lead to the strong cold/moist pool below the boundary cell (see Fig. 20c and is also evident in the doppler winds in Fig. 23), which drives outflow from the transition region at low levels (see Fig. 20e), although we note that significant variability was found from leg SC1 to SC2. The cold pool in SC1 is 20 km in extent with >1 K temperature depression, but that in SC2 consists of two weaker (0.5 K temperature depression) cold pools with more limited horizontal extent. There also appear to be sections of the boundary where a strongly-precipitating boundary cell is not present near to the stratocumulus edge. When the cold/moist pool is evident, the air in it has elevated equivalent potential temperature θ_e (Fig. 20d) since the humidity

increase dominates over the suppression in temperature. Similarly elevated θ_e was found under strongly drizzling open cells in the northeastern Pacific (Van Zanten et al., 2005), and a similar inferences can be made from drizzling data from the southeastern Pacific (Comstock et al., 2005), although Paluch and Lenschow (1991) show a case of drizzling stratocumulus in which fluctuations associated with evaporating precipitation were moist and cool by an amount that almost canceled in θ_e. Smaller and weaker cold pools are also evident in the POC region and the overcast region in this study (Fig. 20d), and these too have elevated θ_e.

Thick clouds in the POC consist of both broad active (turbulent) cumulus clouds containing one or more updraft cores, together with more quiescent cells that may be the decaying remnants of earlier active cells. Figure 22 shows examples of these two types of cells, both of which contain significant drizzle. The strongest echoes appear to be found in the more active cells, although quantifying this is difficult given the limited sample size (visual inspection of Fig. 5 demonstrates how few of the cells are sampled in total). Despite the stronger echoes in the active cells, the precipitation rates appear to be equally high in the quiescent cells, reflecting higher drizzle water masses in these cells. Cloud water content and droplet concentrations are very low in the quiescent cells, so this may represent a more mature stage of the conversion of cloud to drizzle via coalescence, and may also be responsible for much of the accumulation mode aerosol depletion in the ultra-clean layer. However, it should be noted that the largest drizzle drops (volume radii in excess of 100 μm) of all in the cells shown in Figure 22 are actually found in the updraft core of the active cell. Here, drizzle drops may be growing particularly large by being suspended in the upward moving cloud water and growing rapidly via coalescence. Such drops would be expected to fall quite rapidly once the updraft ceases, whereas the drizzle drops in the quiescent cell are smaller and would take longer to reach the ground.

An earlier study of stratocumulus drizzle cells in the same region (Comstock et al., 2005) found that typical lifetimes of large precipitating cells are around two hours. What seems remarkable, if the quiescent cells are indeed decaying cells, is that they can still contain large amounts of condensate. The total condensate in the quiescent cell in Figure 22 is approximately the same as that in the active cell, although much of it is in the form of drizzle drops. The liquid water path is estimated from adiabatic considerations (Sect. 5.3) to be $\sim$500 g m^{-2} for this

cell, while the precipitation rate measured from leg C1 (Fig. 22d) is approximately 30 mm d^{-1}, which would lead to a rainout timescale of 20–30 min, consistent with estimates from Comstock et al. (2005). Thus, without significant updraft activity to replenish the cell, it seems reasonable to interpret the quiescent cell as a decaying remnant of an earlier active cell. It is possible that the ultra-clean layer is partly the result of hydrometeors in the decaying cells slowly sedimenting in quiescent air. The optically-thin stratus in the POC may be remnants of cells that take some time to be completely removed by sedimentation. This is consistent with the fact that most of these optically-thin clouds had radar reflectivities larger than -28 dBZ (see Section 3.3 above).

Another possibility for the quiescent cells is that they represent a marine boundary layer cloud analogue to the trailing stratiform regions found in deep mesoscale convective systems (MCSs). Since the stratiform areas in MCSs form partly as a result of weakening and merging active convective cells (Houze Jr., 2004), this interpretation may not be at odds with the decaying remnant idea above. However, stratiform regions in MCSs are also supported by mesoscale ascent, and there is evidence for that in the quiescent cell in the low frequency (smoothed) vertical wind in Fig. 22f, which shows a 3–4 km wide region where the mean vertical wind is 10–30 cm s^{-1}, which is sufficient to loft 50 µm drizzle particles, similar to the mean volume radius of such drops in the drizzle cell (Fig. 22c). This supports an earlier finding from (Van Zanten and Stevens, 2005) that the drizzling regions in a POC are associated with mean vertical ascent. These mesoscale updrafts may thus prolong the timescale over which drizzle can remain in cloud, and potentially the cloud lifetime itself. Cloud resolving modeling will be useful in determining the importance of broad scale ascent in this context.

To what extent are the precipitating cells inside the POC different from the boundary cells in the transition zone? Figure 5 demonstrates that peak radar reflectivities in the POC cells can be as high as those in the boundary cells. The primary difference, it appears, is the horizontal extent of the precipitation features in the boundary cells (typically 10–20 km wide) in contrast to those in the POC which have a typical scale of $\sim$5 km. That said, the boundary cells in some cases appear to be two distinct cells that are sufficiently close that their precipitating cores overlap (e.g. CB run in Fig. 5). As Figure 8 shows, there do not appear to be marked differences

in either cloud or drizzle condensate amounts in the transition cells and the POC clouds, and drizzle drop sizes and concentrations (Fig. 9c,d) are similar. So it appears that precipitating cells in the POC and the boundary cell differ largely in their horizontal extent and are otherwise quite similar in nature.

9 Conclusions

Aircraft flight legs $\sim$200 km long, from two flights approximately 12 h apart, crossing a spatial transition between a pocket of open cells and the surrounding closed cell stratocumulus, are used in conjunction with satellite data to document aspects of the structure of the cloud, precipitation and aerosol macrostructure and microphysics in the marine boundary layer over the southeast Pacific approximately 1000 km from the Chilean/Peruvian coast. The long flight legs allowed good sampling of both the open and closed cell region, and of the transition between them. This case study was one of several POC studies with a similar sampling strategy by aircraft during VOCALS-REx, and analysis of these cases will provide insight into whether the features observed in this case are ubiquitous POC features or peculiar to this specific case.

Remarkable contrasts in both the macrostructure and the microphysical structure are observed between the open and closed cell regions on both flights. Table 2 serves to describe the key conclusions regarding similarities and differences in the MBL, cloud, precipitation, and aerosol structure between the two regions. In general, these findings echo those of the few existing studies that have sampled POC-overcast transitions (Van Zanten and Stevens, 2005; Petters et al., 2006; Sharon et al., 2006; Comstock et al., 2007), but the comprehensive instrument suite used here is able to quantify these differences with more certainty than before. Because a cloud base precipitation rate of 1 mm d^{-1} is equivalent to $\sim$30 W m^{-2} of cloud layer warming, a particularly pertinent finding here is that persistent drizzle with a magnitude ($\sim$3 mm d^{-1}) comparable to the longwave driving (70–90 W m^{-2} of flux divergence) is present in the overcast region surrounding the POC. Since satellite imagery several hours after the flight shows that the surrounding clouds remained overcast, this suggests that drizzle is *not* a sufficient condition for POC formation. These results make determining the critical factors responsible for POC

formation all the more challenging, but this case is ripe for testing cloud resolving models and using them to explore controls on POC formation.

There are remarkable contrasts, broadly consistent on both flights, in the aerosol physical properties between the overcast and open cell regions. Accumulation mode aerosol concentrations in the subcloud layer are roughly a factor of three higher in the overcast region than in the POC, and the cloud droplet concentrations reflect these strong contrasts with much lower values in the POC than in the overcast region. In the POC, the aerosols are far more vertically stratifed than in the overcast region, with extremely low accumulation mode concentrations in an ultra-clean layer towards the top of the MBL. There is only a very small concentration of particles in the Aitken mode in the overcast region (in contrast to the POC), suggesting that these particles are being activated and removed (perhaps grown to larger sizes by aqueous phase processing). There is significant evidence that coalescence scavenging by precipitation formation in the POC is responsible for the extremely low concentrations of cloud droplets and aerosols found in the ultra-clean layer. Given that mean precipitation rates do not differ strongly between the overcast and POC regions and that coalescence scavening is essentially controlled by the mean rate (Wood, 2006), it seems quite surprising that commensurate depletion is not observed in the overcast region. Cloud resolving models with interactive aerosols will help to establish the reasons for this behavior.

We did not observe the actual formation of the POC in this case, so it is not possible to provide a concrete explanation for its formation. It is very interesting that the POC formed within a swath of clouds with mean LWP on the order of 200-250 g m^{-2} according to the MODIS data in Fig. 10. These are roughly twice the climatological mean values for clouds in this region (e.g. Wood et al., 2008; Toniazzo et al., 2011), and are at the highest end of values observed during VOCALS-REx (Bretherton et al., 2010b). In stratocumulus, since the coalescence scavenging rate approximately scales with cloud thickness to the fourth power (see Eq. 18 in Wood, 2006), or alternatively with the square of the LWP, this implies a very strong increase in CCN loss rate as the LWP increases. We can use Wood (2006) to estimate that the CCN loss rates are 100-160 cm^{-3} day^{-1}, for the observed LWP values, in contrast to climatological mean values roughly four times lower than this. The supply rate of CCN

from the free-troposphere cannot exceed $w_e N_{FT}/z_i$, where w_e is the entrainment rate, N_{FT} is the free-tropospheric potential CCN concentration, and z_i is the MBL depth. Using our estimated w_e value of 0.45 cm s^{-1}, we would need N_{FT} to exceed 350-600 cm^{-3} to provide a supply sufficient to replenish the MBL CCN concentration against coalescence losses. The the *total* aerosol concentration in the FT observed on RF06 was significantly lower than this (Table 5), implying that it is unlikely that the FT source was indeed not sufficient to prevent near-complete CCN loss. This result suggests that stratocumulus clouds with high LWP may be fundamentally unstable to coalescence scavenging, and may hint at the primary mechanism for POC formation, namely the build up of LWP under favorable meteorological conditions. Further work, including examination of other VOCALS POC cases, and numerical modeling work, is required to establish POC formation mechanisms.

However, we can propose a POC formation hypothesis to be tested. Let us assume that the FT provides the only significant source of CCN replenishment, and that all free-tropospheric aerosols (i.e. the CN concentration) can ultimately serve as CCN (either directly upon entrainment into the MBL, or by growing through aqueous phase processing after activation in an anomalously strong updraft). In the VOCALS region, the CN concentration is mostly lower than 300 cm^{-3}, but on occasion reached values of 1000 cm-3 in elevated pollution plumes. We will also assume that the entrainment rates of 0.4 cm-3 are fairly typical for the southeastern Pacific (Wood and Bretherton, 2004). Given these values, we can use Wood (2006) and the adiabatic assumption to estimate the LWP values that are required to produce coalescence loss rates that exceed the free-tropospheric replenishment rates. These are 160 and 300 g m^{-2} for N_{FT}=300 and 1000 cm^{-3} respectively. Therefore, we hypothesize that long-lived stratocumulus clouds with areal mean LWP values of greater than 300 g m^{-3} cannot be sustained against coalescence losses under any conditions found during VOCALS-REx.

Acknowledgements. The authors are extremely grateful to the staff, aircrew, and groundcrew of the Research Aviation Facility at the National Center for Atmospheric Research and those of the FAAM, Direct Flight, and Avalon, who operated the two aircraft used in this study. We would like to thank the instrument scientists and operators from the two aircraft who worked tirelessly to provide high-quality datasets used here, and the staff of the University of Wyoming King Air National Facility for supporting the WCR instrument. In addition, we are indebted to all the scientists involved in the VOCALS Program

for their guidance, discussion, and insights that have helped improve this manuscript. Graham Feingold, Hailong Wang, Jan Kazil, Chris Terai, and Andy Berner are thanked for constructive comments on the results and manuscript. Sandra Yuter made helpful suggestions regarding the conceptual model. US financial support for the analysis presented here is from the National Science Foundation (Grant 0745702). UK financial support was provided by the National Environment Research Council Grant number NE/F019874/1.

References

Ackerman, A. S., Toon, O. B., and Hobbs, P. V.: Dissipation of marine stratiform clouds and collapse of the marine boundary-layer due to the depletion of cloud condensation nuclei by clouds, Science, 262, 226–229, 1993.

Ackerman, A. S., Kirkpatrick, M. P., Stevens, D. E., and Toon, O. B.: The impact of humidity above stratiform clouds on indirect aerosol climate forcing, Nature, 432, 1014–1017, 2004.

Ackerman, A. S., vanZanten, M. C., Stevens, B., Savic-Jovcic, V., Bretherton, C. S., Chlond, A., Golaz, J.-C., Jiang, H., Khairoutdinov, M., Krueger, S. K., Lewellen, D. C., Lock, A., Moeng, C.-H., Nakamura, K., Petters, M. D., Snider, J. R., Weinbrecht, S., and Zulauf, M.: Large-eddy simulations of a drizzling, stratocumulus-topped marine boundary layer, Mon. Weather Rev., 137, 1083–1110, 2009.

Albrecht, B. A.: Aerosols, cloud microphysics, and fractional cloudiness, Science, 245, 1227–1230, 1989.

Austin, P., Siems, S., and Wang, Y.: Constraints on droplet growth in radiatively cooled stratocumulus clouds, J. Geophys. Res., 100, 14231–14242, 1995.

Berner, A. and Bretherton, C. S.: Large-eddy simulation of the VOCALS RF06 pocket of open cells: cloud macrostructure, entrainment and maintenance timescale of microphysical gradients, to be submitted to Atmos. Chem. Phys., 2010.

Brenguier, J.-L. and Wood, R.: Observational strategies from the micro to meso scale, from the Strüngmann Forum Report, Clouds in the Perturbed Climate System: Their Relationship to Energy Balance, Atmospheric Dynamics, and Precipitation, edited by: Heintzenberg, J. and Charlson, R. J., MIT Press ISBN 978-0-262-01287-4, 2009.

Bretherton, C. S., Austin, P., and Siems, S. T.: Cloudiness and marine boundary layer dynamics in the ASTEX lagrangian experiments, Part 2: Cloudiness, drizzle, surface fluxes and entrainment, J. Atmos. Sci., 52, 2724–2735, 1995.

Bretherton, C. S., Uttal, T., Fairall, C. W., Yuter, S. E., Weller, R. A., Baumgardner, D., Comstock, K., and Wood, R.: The EPIC 2001 stratocumulus study, B. Am. Meteor. Soc., 85, 967–977, 2004.

Bretherton, C. S., Uchida, J., and Blossey, P. N.: Slow manifolds and multiple equilibria in stratocumulus-capped boundary layers, J. Adv. Model. Earth Syst., 2, 14, 2010.

Bretherton, C. S., George, R., Wood, R., Allen, G., Leon, D., and Albrecht, B.: Southeast Pacific stratocumulus clouds, precipitation and boundary layer structure sampled along 20S during VOCALS-REx, Atmos. Chem. Phys., 10, 10 639–10 654, 2010.

Brost, R. A., Wyngaard, J. C., and Lenschow, D. H.: Marine stratocumulus layers, Part 2: Turbulence budgets, J. Atmos. Sci., 39, 818–836, 1982.

Caldwell, P., Wood, R., and Bretherton, C. S.: Mixed-layer budget analysis of the diurnal cycle of entrainment in SE Pacific stratocumulus, J. Atmos. Sci., 62, 3775–3791, 2005.

Clarke, A., McNaughton, C., Kapustin, V., Shinozuka, Y., Howell, S., Dibb, J., Zhou, J., Anderson, B., Brekhovskikh, V., Turner, H., and Pinkerton, M.: Biomass burning and pollution aerosol over North America: organic components and their influence on spectral optical properties and humidification response, J. Geophys. Res., 112, D12S18, doi:10.1029/2006JD007777, 2007.

Comstock, K., Wood, R., Yuter, S., and Bretherton, C. S.: Radar observations of precipitation in and below stratocumulus clouds, Q. J. Roy. Meteor. Soc., 130, 2891–2918, 2004.

Comstock, K., Bretherton, C. S., and Yuter, S.: Mesoscale variability and drizzle in Southeast Pacific stratocumulus, J. Atmos. Sci., 62, 3792–3807, 2005.

Comstock, K., Yuter, S. E., Wood, R., and Bretherton, C. S.: The three dimensional structure and kinematics of drizzling stratocumulus, Mon. Weather Rev., 135, 3767–3784, 2007.

Feingold, G. and Siebert, H.: Cloud-aerosol interactions from the micro to the cloud scale, In: Perturbed Clouds in the Climate System, edited by: Heintzenberg, J. and Charlson, R. J., Ernst Strungmann Forum MIT Press, Cambridge, MA, 319–338, Frankfurt Institute for Advanced Study, 2009.

Feingold, G., Boers, R., Stevens, B., and Cotton, W. R.: A modeling study of the effect of drizzle on cloud optical depth and susceptibility, J. Geophys. Res., 102, 13527–13534, 1997.

Frisch, A. S., Fairall, C. W., and Snider, J. B.: Measurement of stratus cloud and drizzle parameters in ASTEX with a Ka band doppler radar and a microwave radiometer, J. Atmos. Sci., 52, 2788–2799, 1995.

Geoffroy, O., Brenguier, J.-L., and Sandu, I.: Relationship between drizzle rate, liquid water path and droplet concentration at the scale of a stratocumulus cloud system, Atmos. Chem. Phys., 8, 4641–4654, doi:10.5194/acp-8-4641-2008, 2008.

Houze Jr., R. A.: Mesoscale convective systems, Rev. Geophys., 42, RG4003,

doi:10.1029/2004RG000150, 2004.
Jonker, H. J. J., Heus, T., and Sullivan, P. P.: A refined view of vertical mass transport by cumulus convection, Geophys. Res. Lett., 35, L07810, doi:10.1029/2007GL0326063, 2008.
Kubar, T. L., Hartmann, D. L., and Wood, R.: Understanding the importance of microphysics and macrophysics for warm rain in marine low clouds: Part I. Satellite observations, J. Atmos. Sci., 66, 2953–2972, 2009.
Liou, K. N. and Ou, S. C.: The role of cloud microphysical processes in climate: an assessment from a one-dimensional perspective, J. Geophys. Res., 94, 8599–8607, 1989.
Martin, G. M., Johnson, D. W., and Spice, A.: The measurement and parameterization of effective radius of droplets in warm stratocumulus clouds, J. Atmos. Sci., 51, 1823–1842, 1994.
Mason, B. J.: Production of rain and drizzle in stratiform clouds, Q. J. Roy. Meteor. Soc., 78, 377–386, 1952.
Mason, B. J.: The physics of clouds, Clarendon Press, Oxford, 1957.
Mason, B. J. and Howorth, B. P.: Some characteristics of stratiform clouds over North Ireland in relation to their precipitation, Q. J. Roy. Meteor. Soc., 78, 226–230, 1952.
Miller, M. A. and Albrecht, B. A.: Surface-based observations of mesoscale cumulus-stratocumulus interaction during ASTEX, J. Atmos. Sci., 52, 2809–2826, 1995.
Nakajima, T., King, M. D., Spinhirne, J. D., and Radke, L. F.: Determination of the optical thickness and effective particle radius of clouds from reflected solar radiation measurements: 2. Marine stratocumulus observations, J. Atmos. Sci., 48, 728–750, 1991.
Nicholls, S.: The dynamics of stratocumulus: aircraft observations and comparisons with a mixed layer model, Q. J. Roy. Meteor. Soc., 110, 783–820, 1984.
Nicholls, S. and Leighton, J.: An observational study of the structure of stratiform cloud sheets: Part 1: Structure, Q. J. Roy. Meteor. Soc., 112, 431–460, 1986.
Paluch, I. R. and Lenschow, D. H.: Stratiform cloud formation in the marine boundary layer, J. Atmos. Sci., 48, 2141–2158, 1991.
Pawlowska, H. and Brenguier, J. L.: An observational study of drizzle formation in stratocumulus clouds for general circulation model (GCM) parameterizations, J. Geophys. Res., 108, 8630, doi:10.1029/2002JD002679, 2003.
Petters, M. D., J. R. Snider, B. Stevens, G. Vali, I. Faloona, and L. Russell: 2005, Accumulation mode aerosol, pockets of open cells, and particle nucleation in the remote subtropical pacific marine boundary layer. J. Geophys. Res., 111, D02206, doi:10.1029/2004JD005694.
Pruppacher, H. R. and Klett, J. D.: Microphysics of Clouds and Precipitation, Series: Atmospheric and

Oceanographic Sciences Library, Vol. 18, Second Revised and Expanded Edition with an Introduction to Cloud Chemistry and Cloud Electricity, Hardcover, Kluwer Academic Publishers, 976 pp., ISBN: 978-0-7923-4211-3, online available at: http://www.springer.com/series/5669, 1997.

Reynolds, R. W. and Smith, T. M.: Improved global sea surface temperature analyses using optimum interpolation., J. Climate, 7, 929–948, 1994.

Rosenfeld, D., Kaufman, Y. J., and Koren, I.: Switching cloud cover and dynamical regimes from open to closed Benard cells in response to the suppression of precipitation by aerosols, Atmos. Chem. Phys., 6, 2503–2511, doi:10.5194/acp-6-2503-2006, 2006.

Savic-Jovcic, V. and Stevens, B.: The structure and mesoscale organization of precipitating stratocumulus, J. Atmos. Sci., 65, 1587–1605, 2008.

Seinfeld, J. H. and Pandis, S. N.: Atmospheric Chemistry and Physics, John Wiley and Sons, Toronto, 1996.

Sharon, T. M., Albrecht, B. A., Jonsson, H., Minnis, P., Khaiyer, M. M., VanReken, T. M., Seinfeld, J., and Flagan, R.: Aerosol and cloud microphysical characteristics of rifts and gradients in maritime stratocumulus clouds, J. Atmos. Sci., 63, 983–997, 2006.

Simpson, G. C.: On the formation of cloud and rain, Q. J. Roy. Meteor. Soc., 67, 99–133, 1941.

Singleton, F.: Aircraft observations of rain and drizzle from layer clouds, Q. J. Roy. Meteor. Soc., 86, 195–204, 1960.

Sorooshian, A., Feingold, G., Lebsock, M., Jiang, H., and Stephens, G.: On the precipitation susceptibility of clouds to aerosol perturbations, Geophys. Res. Lett., 36, L13803, doi:10.1029/2009GL038993, 2009.

Squires, P.: The growth of cloud drops by condensation, 2: The formation of large drops, Aust. J. Sci. Res., 5, 473–499, 1952.

Squires, P.: The microstructure and colloidal stability of warm clouds: 1. The relation between structure and stability, Tellus, 10, 256–261, 1958a.

Squires, P.: The microstructure and colloidal stability of warm clouds: 2. The causes of the variations in microstructure, Tellus, 10, 262–271, 1958b.

Stevens, B. and Feingold, G.: Untangling aerosol effects on clouds and precipitation in a buffered system, Nature, 461, 607–613, 2009.

Stevens, B., Cotton, W. R., Feingold, G., and Moeng, C.-H.: Large-eddy simulations of strongly precipitating, shallow, stratocumulus-topped boundary layers, J. Atmos. Sci., 55, 3616–3638, 1998.

Stevens, B., Vali, G., Comstock, K., Wood, R., VanZanten, M., Austin, P. H., Bretherton, C. S., and Lenschow, D. H.: Pockets of Open Cells (POCs) and drizzle in marine stratocumulus, B. Am. Mete-

orol. Soc., 86, 51–57, 2005.
Tomlinson, J., Li, R., and Collins, D. R.: Physical and chemical properties of the aerosol within the south-eastern Pacific marine boundary layer, J. Geophys. Res., 111, D12211, doi:10.1029/2006JD007771, 2007.
Toniazzo, T., Wood, R., and coauthors: Large-scale and synoptic meteorology in the south-east Pacific during VOCALS Regional Experiment, October/November 2008, Atmos. Chem. Phys. Disc., 11, 225-288, 2011.
Vali, G., Kelly, R. D., French, J., S H., Leon, D., and McIntosh, R. E., and Pazmany, A.: Finescale structure and microphysics of coastal stratus, J. Atmos. Sci., 55, 3540–3564, 1998.
Van Zanten, M. C. and Stevens, B.: Observations of the structure of heavily precipitating marine stratocumulus, J. Atmos. Sci., 62, 4327–4342, 2005.
Van Zanten, M. C., Stevens, B., Vali, G., and Lenschow, D.: Observations of drizzle in nocturnal marine stratocumulus, J. Atmos. Sci., 62, 88–106, 2005.
Wang, H. and Feingold, G.: Modeling mesoscale cellular structures and drizzle in marine stratocumulus, Part 2: The microphysics and dynamics of the boundary region between open and closed cells, J. Atmos. Sci., 66, 3257–3275, 2009.
Wang, S., Albrecht, B. A., and Minnis, P.: A regional simulation of marine boundary layer clouds, J. Atmos. Sci., 50, 4022–4043, 1993.
Wendisch, M., Garrett, T. J., and Strapp, J. W.: Wind tunnel tests of the airborne PVM-100A response to large droplets, J. Atmos. Ocean. Tech., 19, 1577–1584, 2002.
Wood, R.: Parametrization of the effect of drizzle upon the droplet effective radius in stratocumulus clouds, Q. J. Roy. Meteor. Soc., 126, 3309–3324, 2000.
Wood, R. and C. S. Bretherton, 2004: Boundary layer depth, entrainment and decoupling in the cloud-capped subtropical and tropical marine boundary layer. J. Climate, 17, 3576–3588, 2004.
Wood, R.: Drizzle in stratiform boundary layer clouds: Part I. Vertical and horizontal structure, J. Atmos. Sci., 62, 3011–3033, 2005.
Wood, R.: The rate of loss of cloud droplets by coalescence in warm clouds, J. Geophys. Res., 111, D21205, doi:10.1029/2006JD007553, 2006.
Wood, R.: Cancellation of aerosol indirect effects in marine stratocumulus through cloud thinning, J. Atmos. Sci., 64, 2657–2669, 2007.
Wood, R., Bretherton, C. S., Mechoso, C. R., Weller, R. A., and Huebert, B. and coauthors: The VAMOS Ocean-Cloud-Atmosphere-Land Study Regional Experiment (VOCALS-REx): goals, platforms, field operations, and meteorological context, Atmos. Chem. Phys., 2011.

Wood, R. and Hartmann, D. L.: Spatial variability of liquid water path in marine boundary layer clouds: The importance of mesoscale cellular convection, J. Climate, 19, 1748–1764, 2006.

Wood, R. and Taylor, J. P.: Liquid water path variability in unbroken marine stratocumulus, Q. J. Roy. Meteor. Soc., 127, 2635–2662, 2001.

Wood, R., Comstock, K. K., Bretherton, C. S., Cornish, C., Tomlinson, J., Collins, D. R., and Fairall, C.: Open cellular structure in marine stratocumulus sheets, J. Geophys. Res., 113, D12207, doi:10.1029/2007JD009596, 2008.

Wood, R., Köhler, M., Bennartz, R., and O'Dell, C.: The diurnal cycle of surface divergence over the global oceans, Q. J. Roy. Meteor. Soc., 135, 1484–1493, 2009a.

Wood, R., Kubar, T., and Hartmann, D. L.: Understanding the importance of microphysics and macrophysics for warm rain in marine low clouds: Part 2. Heuristic models of rain formation, J. Atmos. Sci., 66, 2973–2990, 2009b.

Xue, Y., Wang, L. P., and Grabowski, W. W.: Growth of cloud droplets by turbulent collision-coalescence, J. Atmos. Sci., 65, 331–356, 2008.

Zuidema, P. and coauthors: Microwave radiometer retrievals in VOCALS (tent.), Atmos. Chem. Phys., p. in preparation, 2010.

Table 1. Overview of C-130 flight legs, and the earlier BAe-146 flight legs. SC: subcloud leg; CB: leg around cumulus cloud base level; C: leg near the center of the stratocumulus cloud layer; AC: above cloud leg in the free-troposphere above the marine inversion; S: sawtooth run from above inversion to base of cloud. The mean run altitude z is given. Directions are given as from POC to overcast (P→O) or vice-versa. Times are in UTC (LT+3 h). Run lengths L in the three different regions are given in kilometers.

Leg	z [m]	times [UTC]	direction	L (POC) [km]	L (Overcast) [km]	L (Transition) [km]
BAe-146 legs, B409, 27 Oct 2008[a]						
B-AC	1490	21:42:00–22:02:24	P→O	–	–	–
B-SC	314	22:06:50–22:40:00	O→P→O	69	102	–
B-C	1172	22:46:40–23:04:40	O→P→O	–	–	–
C-130 legs, RF06, 28 Oct 2008						
AC	1584	08:33:15–09:03:02	O→P	109	86	16
SC1	145	09:09:03–09:39:00	P→O	92	85	23
CB	623	09:42:10–10:12:10	O→P	88	79	25
C1	1157	10:15:16–10:45:40	P→O	75	109	28
S	1040–1640	10:56:40–11:33:40	O→P	107	104	43
SC2	146	11:41:00–12:15:41	P→O	137	74	22
C2	1084	12:19:50–12:50:55	O→P	97	83	19

[a] Boundaries between POC and overcast could only be clearly defined for the subcloud layer SC leg. In addition, it was impossible to clearly define a transition region on this flight.

Table 2. Key characteristics of the MBL, cloud, precipitation, and aerosol structure in the POC and the overcast region

Characteristic	POC region	Overcast region
MBL structure	Weakly stratified layer above a ∼600 m deep well-mixed surface layer . Temperature and humidity more variable, particularly associated with precipitation near surface in cold/moist pools.	Well-mixed MBL, little evidence of cold pools.
Cloud macrostructure	Highly variable (and bimodal) cloud base and thickness. Cumulus clouds growing from top of subcloud layer and spreading to form stratus, some very thin.	Typical of stratocumulus with well-developed mesoscale cells. Narrow distribution of cloud base and thickness.
Cloud cover	∼60%	Almost 100%
Liquid water	LWP strongly skewed with tail of high values and numerous low values. High fraction of liquid water is in the form of drizzle drops.	LWP has narrow distribution, similar means for clouds in overcast and POC. Most liquid water in cloud droplets.
Precipitation occurrence	45%, 25% and 7% for $Z_{\max}>-15$, $0,10$ dBZ, respectively.	95%, 25% and 2% for $Z_{\max}>-15$, $0,10$ dBZ, respectively.
Precipitation, nature	Almost all clouds drizzling, heavy drizzle common and significant fraction (∼half) reaching surface.	Almost all clouds drizzling, most drizzle moderate and does not reach surface.
Cloud microphysics	Very low and highly variable cloud droplet concentrations (N_{d} from 0.1–40 cm^{-3}), highest values in intermittent active cumulus cells.	Typical of clean marine stratocumulus and relatively uniform (N_{d} from 50–100 cm^{-3}) but decreasing consistently and sharply within 30 km of the transition region.
Aerosols	Low concentrations in the accumulation mode. Strong vertical stratification, with almost no accumulation mode in the upper MBL. More Aitken mode particles than in the overcast region at all levels in the MBL.	Vertically uniform, values fairly typical for clean marine conditions. Low concentration of Aitken mode particles.

Table 3. Various large scale conditions during BAe-146 Flight B409. For some variables, values are given separately for POC and overcast, while for some only an average over a broader region is permissible.

Variable	Platform	Run/Area	Units	POC	Overcast	Both regions
Surface temperature, SST						
SST	BAe-146	SC	C	17.9	18.0	18.0
SST	Reynolds[a]	77–79° W, 20–22° S	C	–	–	17.2
Air temperature and humidity						
T_0	BAe-146[b]	10 m	C	17.0	17.2	–
θ_0	BAe-146	surface	K	288.4	288.7	–
q_0	BAe-146[c]	10 m	g kg^{-1}	7.8	8.1	–
RH_0	BAe-146	10 m	%	65	66	–
θ_{FT}	BAe-146	(z_i+200 m)	K	303.2	305.0	–
θ (z_i^-)	BAe-146	inversion base	K	–	–	289.5
q_{FT}	BAe-146	(z_i+200 m)	g kg^{-1}	–	–	0.35
Winds, pressure						
u,v winds	BAe-146	315 m	m s^{-1}	[−3.1,9.6]	[−3.6,8.8]	–
wind speed, U_{10}	BAe-146[d]	10 m	m s^{-1}	7.7	7.2	–
u,v winds	Quikscat[e]	10 m	m s^{-1}			[−3.2,6.7]
Surface pressure	BAe-146	surface	hPa	1020.2	1020.0	–
u,v winds	BAe-146	mean over MBL	m s^{-1}	–	–	[−4.2,8.5]
Surface fluxes						
LHF	BAe-146, bulk[f]	surface	W m^{-2}	131	116	–
SHF	BAe-146, bulk	surface	W m^{-2}	10	8	–
MBL depth						
Inversion base height z_i	BAe-146	Profiles[g]	m	–	–	1280

[a] Daily mean value from Reynolds and Smith (1994), data available from NOAA ESRL.
[b] Mean air temperature at 10 m altitude estimated using SC and assuming a dry adiabat.
[c] Assumed to be equal to mean vapor mixing ratio on SC.
[d] Estimated using log-wind profile with surface roughness 1.86×10^{-4} m.
[e] Daily mean value for 27 Oct 2008 from Remote Sensing Systems.
[f] Estimated using COARE bulk formula with transfer coefficient of $(1.1+0.01U_{10})\times10^{-3}$.
[g] Estimated from all BAe-146 temperature profiles.

Table 4. Large scale and forcing conditions during C-130 Flight RF06. For some variables, values are given separately for POC and overcast, while for some only an average over a broader region is permissible.

Variable	Platform	Run/Area	Units	POC	Overcast	Both regions
		Surface temperature, SST				
SST	C-130[a]	SC1/SC2	C	17.5	18.0	17.7
SST	AMSR[b]	79–81° W, 16–20° S	C	–	–	17.5
SST	Reynolds[c]	79–81° W, 16–20° S	C	–	–	17.4
		Air temperature and humidity				
T_0	C-130[d]	10 m	C	16.4	17.3	–
θ_0	C-130	surface	K	288.1	289.0	–
q_0	C-130[e]	10 m	g kg^{-1}	8.5	7.6	–
RH_0	C-130	10 m	%	73	60	–
θ_{FT}	C-130	(z_i+200 m)	K	304.1	305.5	–
$\theta\ (z_i^-)$	C-130	inversion base	K	292.3	291.0	–
q_{FT}	C-130	(z_i+200 m)	g kg^{-1}	0.5	0.3	–
		Infrared Radiation				
$F\downarrow/F\uparrow/F\downarrow-F\uparrow$	C-130	AC (z_i+200 m)	W m^{-2}	225/371/−146	233/354/−120	230/363/−133
$F\downarrow/F\uparrow/F\downarrow-F\uparrow$	C-130	SC1/SC2 (z=145 m)	W m^{-2}	302/376/−74	350/379/−29	322/377/−55
ΔF	C-130	(z_i+200 m) – (145 m)	W m^{-2}	−72	−91	−78
		Winds, pressure				
u,v winds	C-130	145 m	m s^{-1}	[−6.8,8.9]	[−7.3,8.3]	–
wind speed, U_{10}	C-130[f]	10 m	m s^{-1}	9.0	8.8	–
u,v winds	Quikscat[g]	10 m	m s^{-1}			[−6.3,6.7]
Surface pressure	C-130	surface	hPa	1018.2	1017.6	–
u,v winds	C-130	mean over MBL	m s^{-1}	–	–	[−7.4,8.3]
		Surface fluxes				
LHF	C-130, bulk[h]	surface	W m^{-2}	122	160	–
SHF	C-130, bulk	surface	W m^{-2}	15	9	–
SHF	C-130, eddy corr.[i]	surface	W m^{-2}	12	4	–
		Large scale surface divergence, subsidence, and MBL depth				
du/dx, dv/dy	Quikscat[j]	78–82° W,15–21° S	s^{-1}	–	–	[3.3,−1.6]×10^{-6}
D_0=du/dx+dv/dy	Quikscat	78–82° W,15–21° S	s^{-1}	–	–	1.67×10^{-6}
w_{850}	Quikscat[k]	78–82° W,15–21° S	cm s^{-1}	–	–	−0.25
w_{850}	NCEP reanalysis[l]	78–82° W,15–21° S	cm s^{-1}	–	–	−0.20
Inversion base height z_i	C-130	Profiles[m]	m	1375	1375	–
Cloud top height	C-130	WCR[n]	m	1347	1363	–

[a] A correction of −1.0 C has been added to the nadir IR radiometer on the C-130 based on multi-flight comparison with Reynolds SST.

[b] Advanced Microwave Scanning Radiometer on the NASA Aqua satellite, data taken at 0130 LT.

[c] Daily mean value from Reynolds and Smith (1994), data available from NOAA ESRL.

[d] Mean air temperature at 10 m altitude estimated using SC1 and SC2 and assuming a dry adiabat.

[e] Assumed to be equal to mean vapor mixing ratio on SC1/SC2.

[f] Estimated using log-wind profile with surface roughness 1.86×10^{-4} m.

[g] Daily mean value for 28 Oct 2008 from Remote Sensing Systems.

[h] Estimated using COARE bulk formula with transfer coefficient of (1.1+0.01U_{10})×10^{-3}.

[i] Eddy correlation not available for LHF because the high-rate hygrometer was not functional.

[j] Daily mean value for 28 Oct 2008.

[k] Assuming constant divergence from the surface to 850 hPa.

[l] Daily mean value for 28 Oct 2008.

[m] Estimated from all C-130 temperature profiles.

[n] Median values of cloud top from SC1, SC2, AC and CB legs.

Table 5. Mean cloud microphysical parameters for the POC, overcast, and transition regions during RF06. Aerosol concentrations are mean values for drizzle-free clear-air samples, screened using the criteria described in Sect. 2.4. The volatile fraction f_{volatile} is estimated from the leg means as $(N_{\mathrm{CN}}-N_{\mathrm{CN,hot}})/N_{\mathrm{CN}}$. Cloud droplet and concentrations N_{d} and effective radii r_{e} are for cloudy samples only. A minimum of 20 samples (1 Hz) is required to include a mean in the table; data for regions/levels with fewer than 20 samples are not presented.

Variable (size, instruments)	Units	Level (height, legs)	POC	Transition	Overcast
Cloud microphysical properties (in-cloud)					
N_{d} ($1<r<23.5$ µm, CDP)	cm^{-3}	Cloud base (623 m, CB)	21	23	†
		Cloud level (1120 m, C1/C2)	7	18	70
r_{e} ($1<r<23.5$ µm, CDP	µm	Cloud base (623 m, CB)	8.9[22.5]	10.2[50.5]	†
and [...] $1<r<800$ µm, CDP/2-D-C)		Cloud level (1120 m, C1/C2)	17.6[38.8]	16.2[37.4]	10.2[13.4]
Aerosol properties (clear air)					
N_{a} ($0.12<D<3.12$ µm, PCASP)	cm^{-3}	Subcloud (145 m, SC1/SC2)	31	¶	95
		Cloud base (623 m, CB)	17	¶	84
		Cloud level (1120 m, C1/C2)	2	2	¶
		Free-troposphere (1584 m, AC)	49	31	47
N_{CN} ($D>10$ nm, TSI 3760)	cm^{-3}	Subcloud (145 m, SC1/SC2)	151	¶	140
		Cloud base (623 m, CB)	235	¶	145
		Cloud level (1120 m, C1/C2)	75	200	¶
		Free-troposphere (1584 m, AC)	292	306	274
$N_{\mathrm{CN,hot}}$ ($D>10$ nm, TSI 3010)	cm^{-3}	Subcloud (145 m, SC1/SC2)	47	¶	101
		Cloud base (623 m, CB)	109	¶	108
		Cloud level (1120 m, C1/C2)	25	34	¶
		Free-troposphere (1584 m, AC)	124	92	141
f_{volatile} ($D>10$ nm)	cm^{-3}	Subcloud (145 m, SC1/SC2)	0.69	¶	0.28
		Cloud base (623 m, CB)	0.54	¶	0.25
		Cloud level (1120 m, C1/C2)	0.67	0.83	¶
		Free-troposphere (1584 m, AC)	0.58	0.70	0.49

¶ No clear-air data
† No cloud data

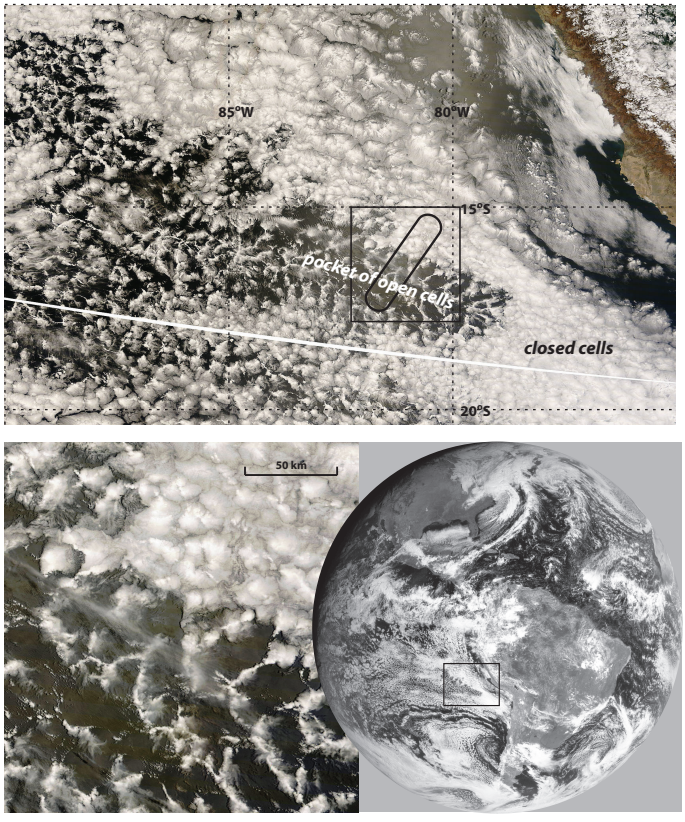

Fig. 1. Visible satellite images on 28 October 2008 showing boundary between region of closed and open cells that was sampled by the aircraft during RF06. Anticlockwise from bottom right: GOES-10 visible image from 15:00 UTC; MODIS visible imagery from 15:50 UTC; blow-up of MODIS visible imagery from 15:50 UTC. The oval in the upper panel represents an oval containing the location of the C-130 measurements, advected using the mean MBL winds as described in the text.

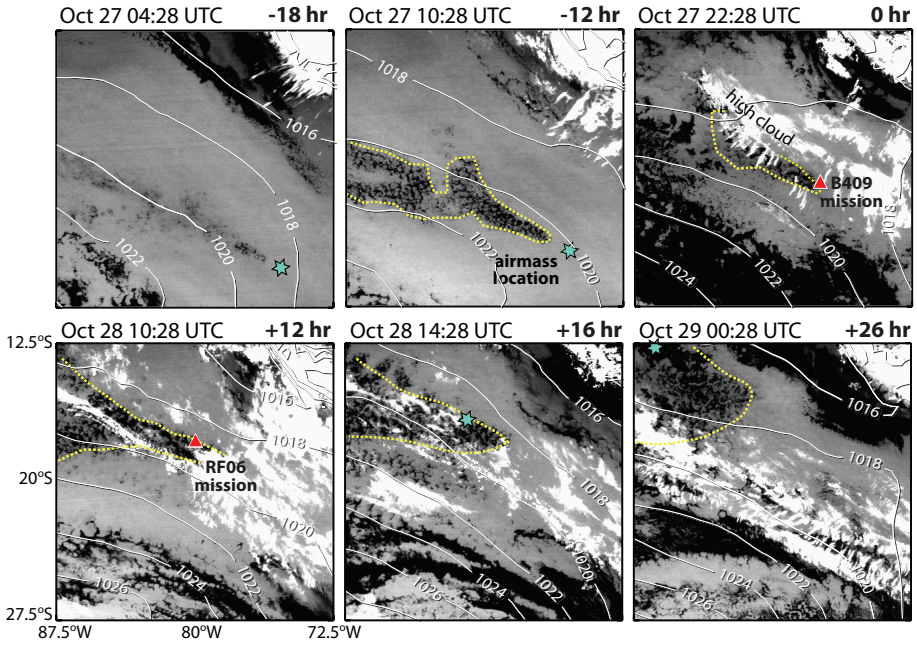

Fig. 2. Sequence of thermal infrared satellite images from GOES-10 for a 44 h period from 04:26 UTC on 27 October (18 h before flight B409) to 00:28 UTC on 29 October 2008 (12 h after the end of the sampling on flight RF06). The blue stars (or red triangles for times of missions) show the location of the advected airmass over the period determined using forward/backward Hysplit trajectories initialized at 00:00 UTC 28 October. White contours show sea level pressure contours, while yellow dashed line delineates region of open cells. Although not discussed further in this manuscript, the yellow boat indicates the location of the NOAA R/V Ronald H Brown which sampled the same pocket of open cells but at a more westward location near 20°S, 85° during the first half of 27 October.

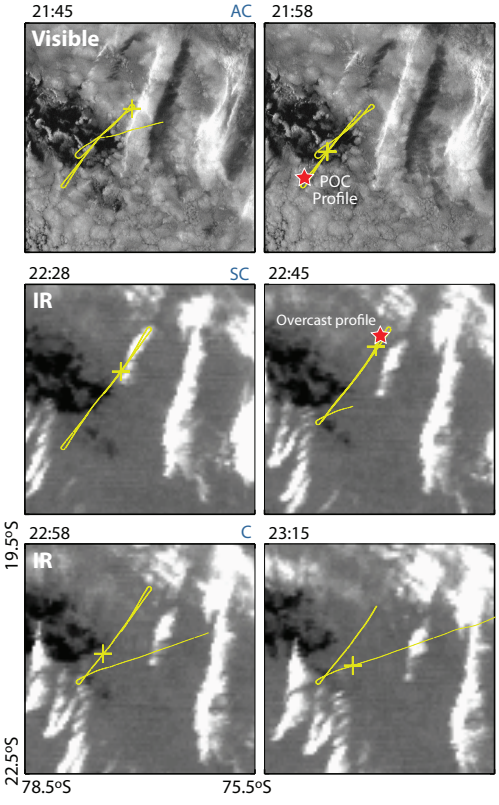

Fig. 3. GOES visible imagery (upper row) and infrared imagery (lower two rows) between 21:45 UTC and 23:15 UTC 27 October with near-coincident hour-long sections (yellow) of the BAe-146 flight track during B409, centered on the image time overlaid. The yellow cross shows the location of the aircraft at the time of the image, with the image time shown at top left of the panels. The aircraft leg closest to the image time is given in blue text at top right of panel. The red stars represent the approximate location of the aircraft during two profiles.

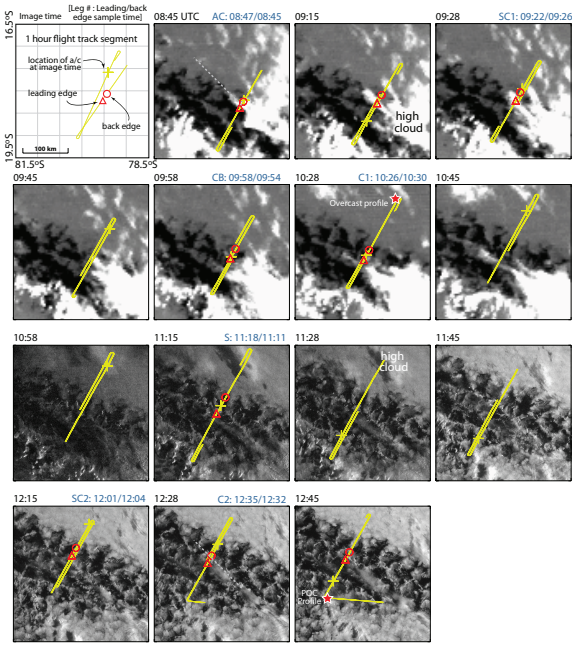

Fig. 4. GOES IR imagery (upper two rows) and visible imagery (lower two rows) between 08:45 UTC and 12:45 UTC 28 October with near-coincident hour-long sections (yellow) of the C-130 flight track during RF06, centered on the image time overlaid. The yellow cross shows the location of the aircraft at the time of the image, with the image time shown at top left of the panels. The aircraft track before and after the image time is advected using the mean low level flow determined from the aircraft data to account for cloud motion. The red triangle and circle show locations of the leading and back edges of the transition region, respectively (see text), and are plotted on the run most closely coincident with the satellite data (run given in blue text at top right of panel, with times showing when the leading/back edge was crossed. The red stars represent the approximate location of the aircraft during the two representative profiles used to characterize the vertical structure in the POC and overcast regions. The gray dashed line in the 08:45 and 12:28 panels shows the track of the leading edge sampled at 08:45 if it were advected with the mean MBL winds for the approximately 3.75 hours between these two times.

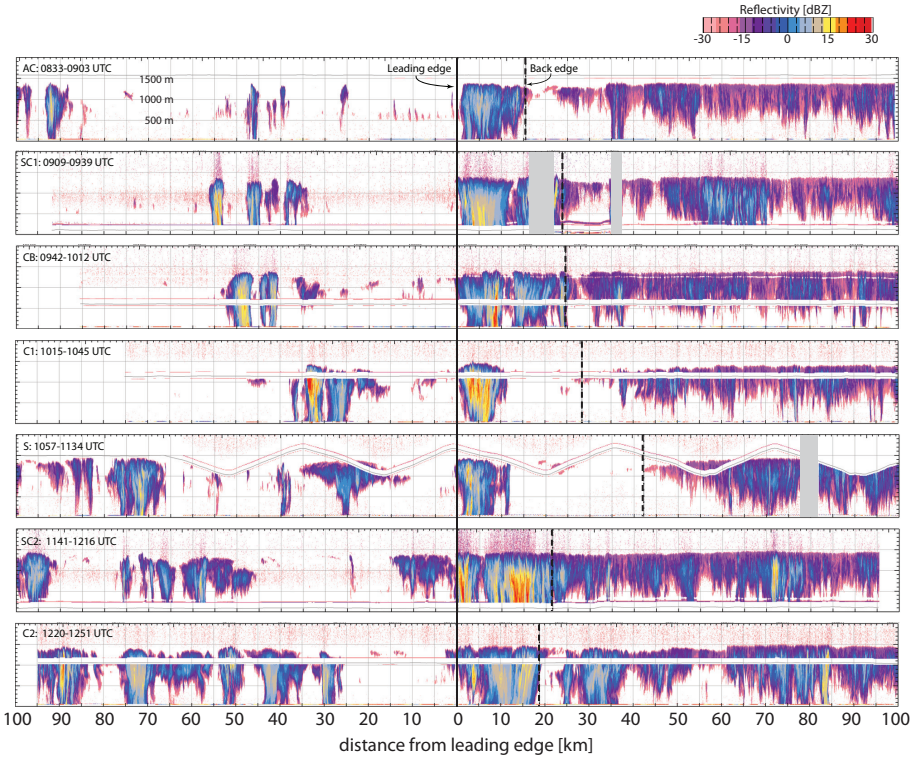

Fig. 5. Radar cross sections from the WCR for all legs in RF06. Runs are presented in time order (earliest at top). Gray regions denote periods when WCR was not functional.

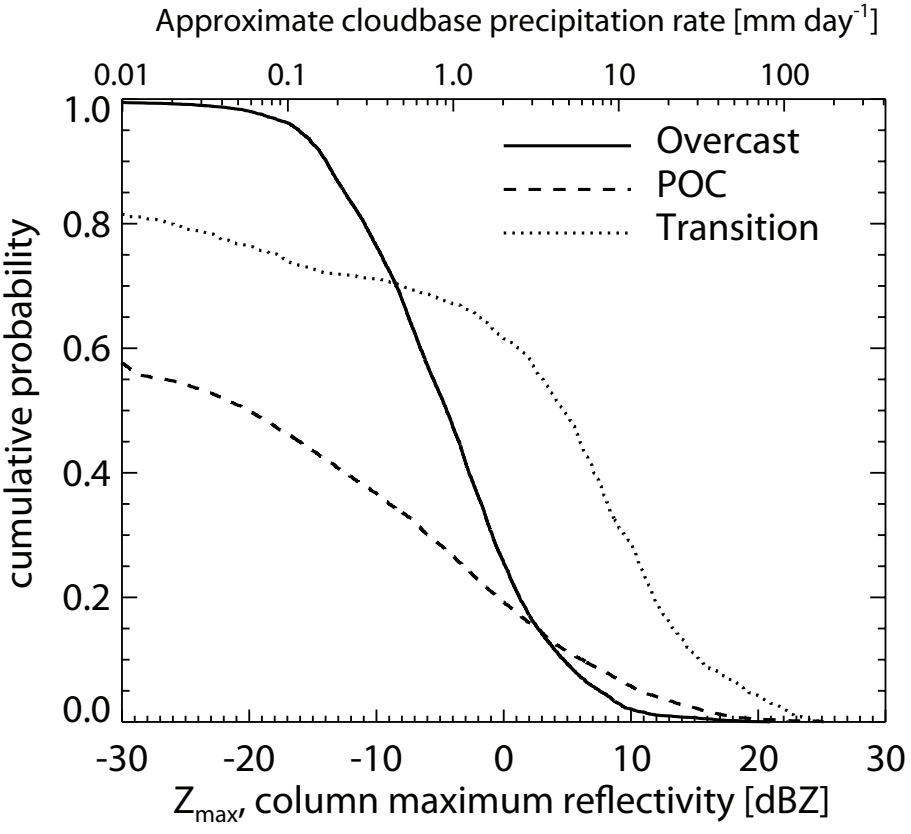

Fig. 6. Cumulative probability of column maximum radar reflectivity Z_{max} greater than the abscissal value, for the overcast (solid), POC (dashed), and transition (dotted) regions. All available WCR data from all flight legs were used to construct the plot. The top axis denotes the approximate cloudbase precipitation rate corresponding to Z_{max} constructed using the Z–R relationship discussed in Sect. 2.3.

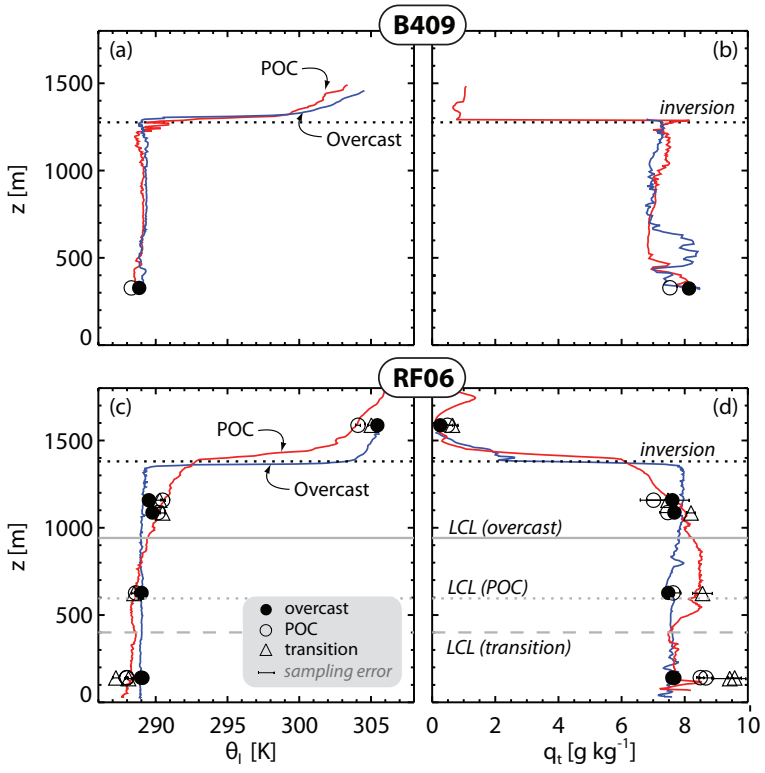

Fig. 7. Profiles from RF06 of mean values of **(a,c)** liquid potential temperature and **(b,d)** total water content, from straight and levels runs (symbols) in the POC, overcast, and transition regions. Data from both flight B409 **(a,b)** and flight RF06 **(c,d)** are shown. For B409, the two available profiles are shown. For RF06 representative example profiles are also shown for the POC (red, 120 km from leading edge, 12:55–13:05 UTC) and overcast (blue, 160 km from leading edge, 10:50–10:56 UTC) regions. Mean lifting condensation levels (LCLs) determined from the subcloud runs are shown for RF06 case. Profile locations are shown in Figs. 3 and 4.

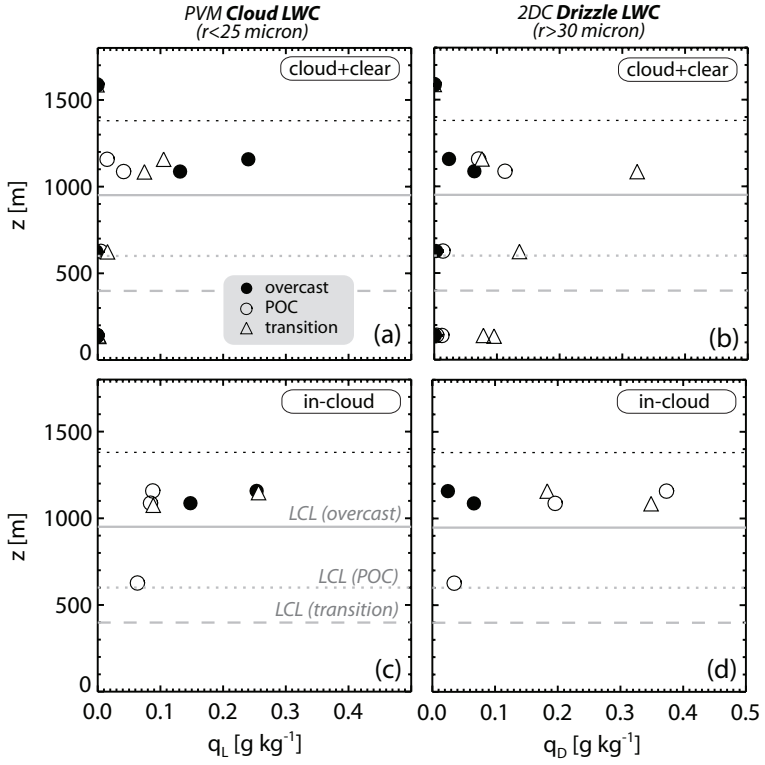

Fig. 8. Profiles from RF06 of mean values of cloud **(a,c)** and drizzle **(b,d)** liquid water content from straight and levels runs (symbols) in the POC, overcast, and transition regions. The upper panels **(a,b)** give values averaged over both cloudy and clear portions of the legs, while the lower panels **(c,d)** show values averaged over cloudy samples only. Note that there is little difference between the cloud+clear and in-cloud values for the overcast region since the runs were either almost entirely in cloud or entirely out of cloud.

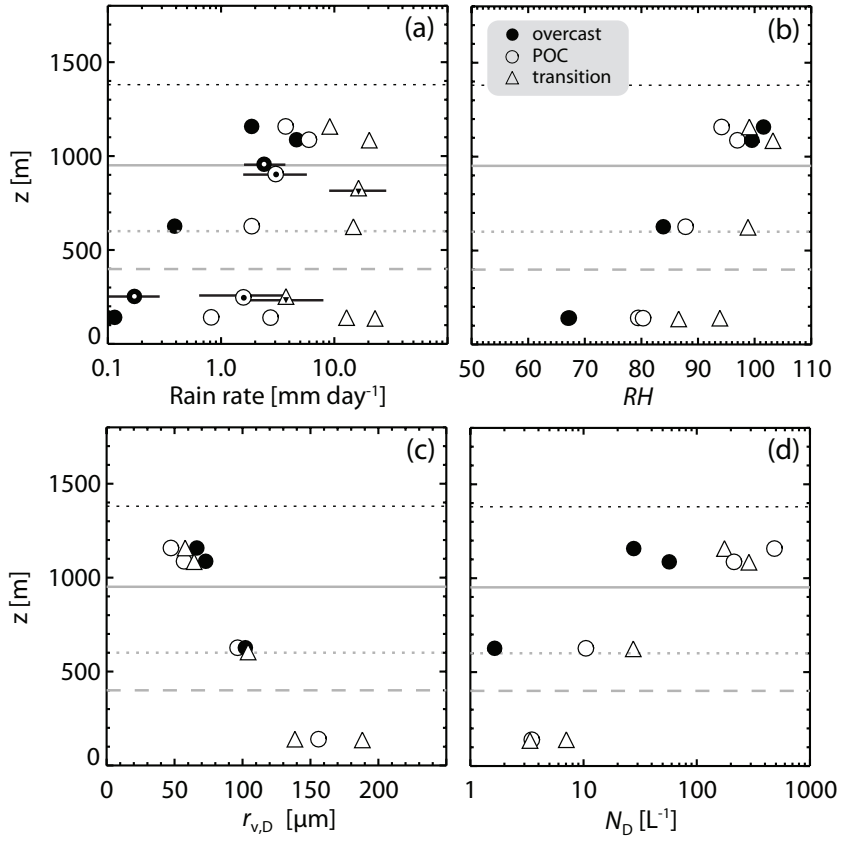

Fig. 9. Profiles from RF06 of mean values of **(a)** precipitation rate (radar estimated values are shown for the height of maximum reflectivity and at 250 m by symbols with dots and horizontal bars show leg-leg variability), **(b)** relative humidity, **(c)** volume radius of drizzle drops, and **(d)** drizzle drop concentration in samples where the drizzle concentration exceeds 1 L^{-1}. Symbolia are the same as for Fig. 7.

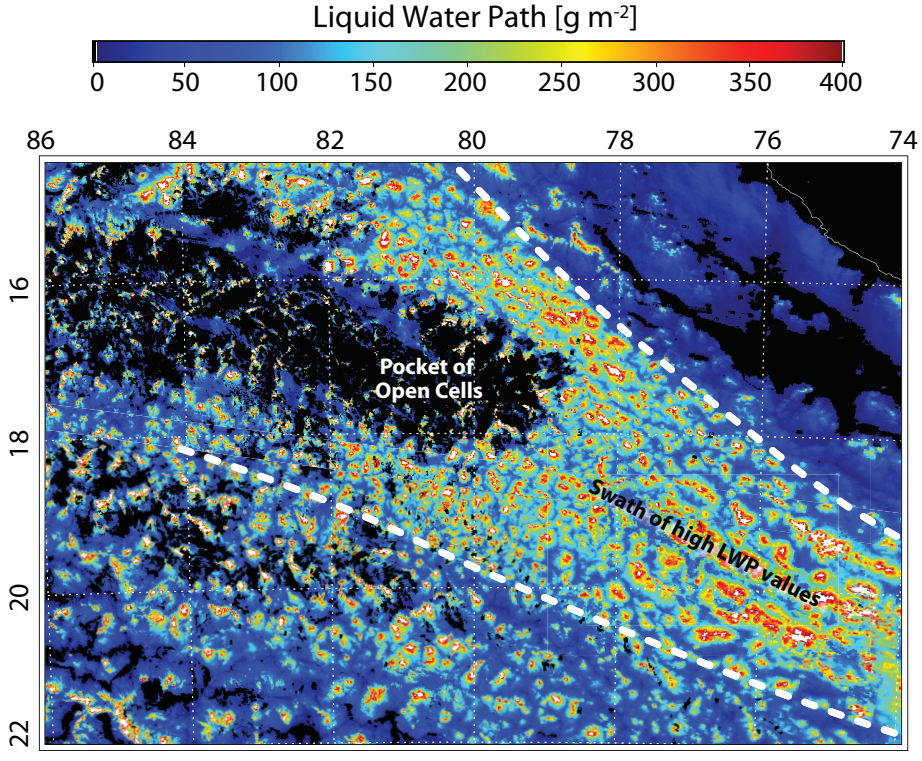

Fig. 10. MODIS-estimated cloud liquid water path (LWP) for the same overpass (15:50 UTC, 28 October 2008) as shown in Fig. 1.

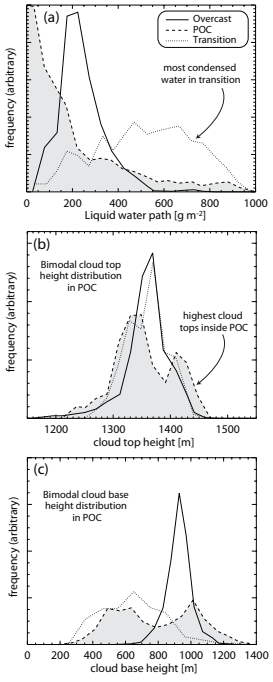

Fig. 11. Probability distribution functions from RF06 for **(a)** liquid water path; **(b)** cloud top height; **(c)** cloud base height, for overcast, POC, and transition regions. Cloud base height data are from the WCL. LWP data are from the microwave radiometer data on the two subcloud legs. Cloud top height data are from the WCR on the subcloud, above-cloud, and cloud-base legs. Cloud-level legs were not used to prevent the chance of the cloud top occurring in the radar dead-zone. Cloud base data are from the two subcloud legs. In heavy drizzle the lidar algorithm is unable to detect a clear cloud base, and in these cases we use the height of the maximum radar reflectivity as a proxy for the cloud base. For the POC and transition regions this substitution accounts for roughly 50% of all data points, while for the overcast radar data are used only 5% of the time.

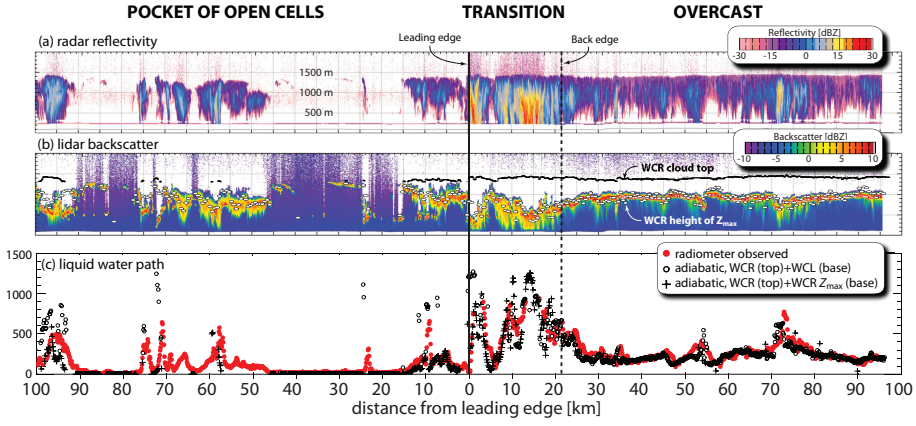

Fig. 12. Time series, from leg SC2 of RF06, of **(a)** WCR radar reflectivity; **(b)** WCL lidar backscatter, with WCR cloud top (1 Hz) and the height of the maximum WCR reflectivity (ovals, smoothed with 7 s triangular filter and plotted every fifth point for clarity) overlaid; **(c)** liquid water path from the microwave radiometer (red circles) and estimated using two adiabatic models. Both models use the WCR observed cloud top height, but one uses the lidar-derived cloud base height where available (open circles), and the other uses the height of the maximum WCR radar reflectivity as a proxy for the cloud base height (crosses) where strong drizzle precludes accurate WCL cloud base height estimates.

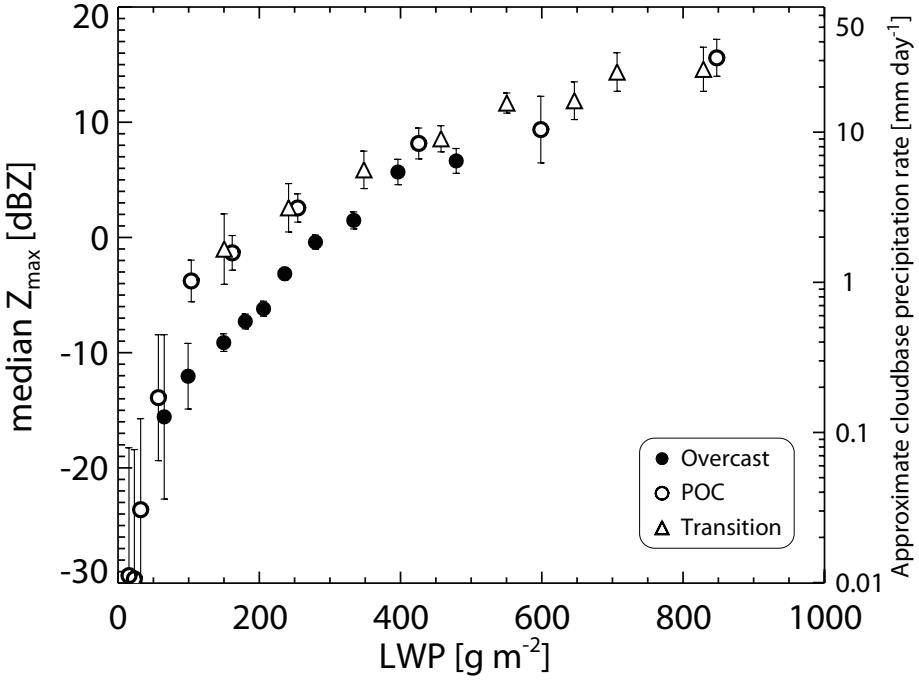

Fig. 13. Median column maximum reflectivity $Z_{\max}$ for all samples on which the WCL detected clouds above, binned as a function of LWP in the overcast (solid circles), POC (open circles), and transition (open triangle) regions. All data from the two RF06 subcloud legs SC1 and SC2 are used. The right axis denotes the approximate cloudbase precipitation rate corresponding to $Z_{\max}$ constructed using the Z–R relationship discussed in Sect. 2.3. Error bars show approximate 95% confidence limits on plotted means.

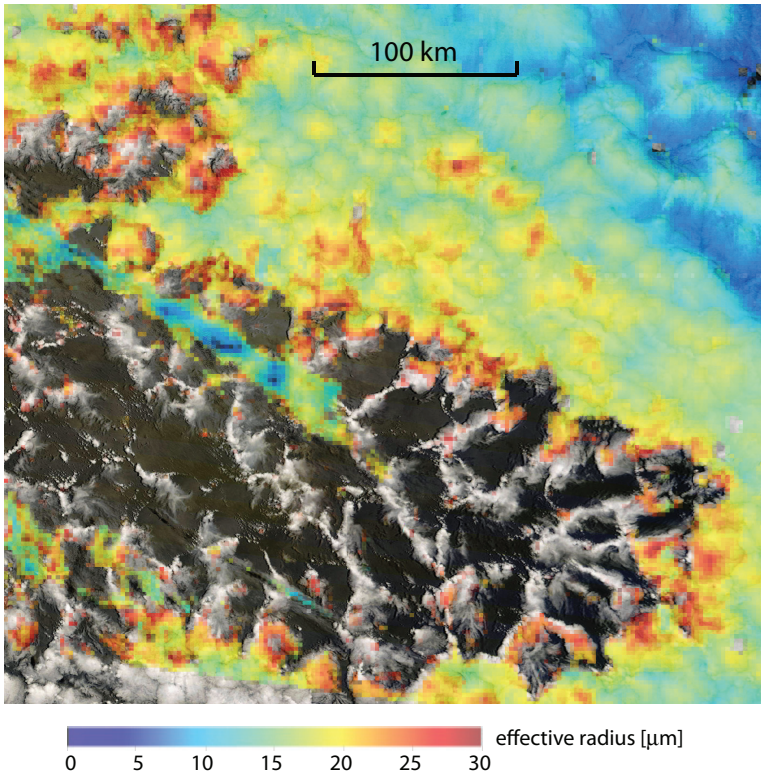

Fig. 14. MODIS-estimated cloud top effective radius r_e (colors) from the 2.1 μm near-IR channel, overlaid on MODIS 250 m visible imagery which is revealed where r_e retrievals are not performed because 1 km pixels used for the retrieval are determined to be partially filled, too optically thin, or are cloud edge pixels.

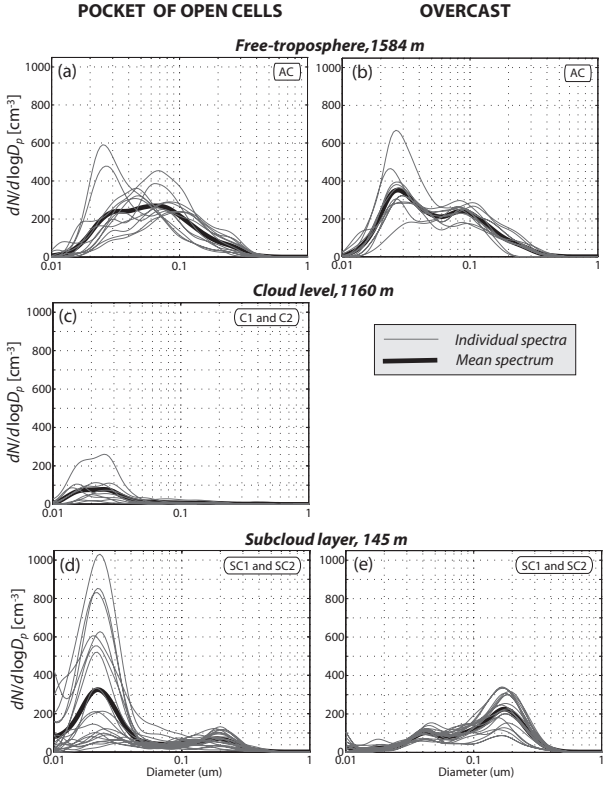

Fig. 15. Aerosol size distributions from RF06 for clear-air samples measured with the University of Hawaii in-cabin sampling system, at different levels in the POC region (**a**,**c**,**d** for the free-troposphere, cloud level, and subcloud layer, respectively) and for the overcast region (**b** and **e** for the free-troposphere and subcloud layers, respectively). We show both individual spectra (typically taken over 10 s samples) and the mean spectrum for each level/region, to emphasize variability. No data are available from the cloud level in the overcast region since almost the entire leg was cloudy.

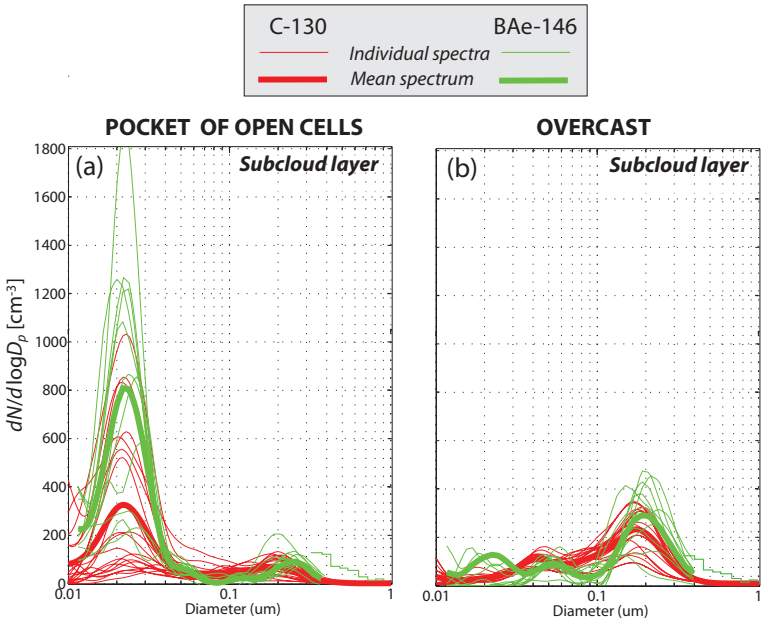

Fig. 16. Aerosol size distributions from the BAe-146 in B409 (green) and from the C-130 in RF06 (red) for clear-air samples in the subcloud layer of **(a)** the POC and **(b)** the overcast region. Both individual spectra (typically taken over 10 s samples) and the mean spectrum for each level/region are shown as per Fig. 15.

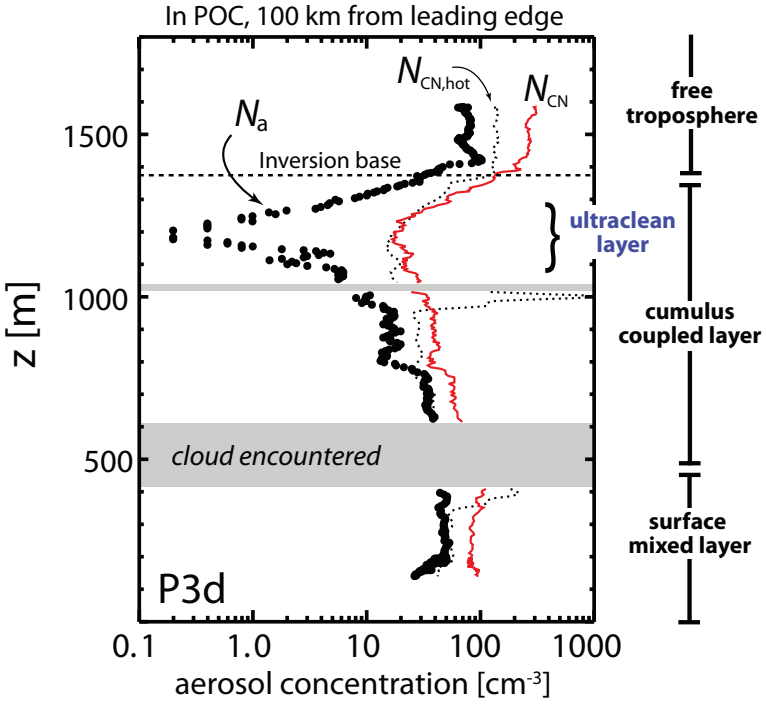

Fig. 17. Representative profile (Profile 3d from RF06) within the POC of aerosol concentration N_a measured with the PCASP (solid circles), the CN counter (red) and with the CN counter after heating to 250 C (short-dash) in the POC region approximately 100 km from the leading edge.

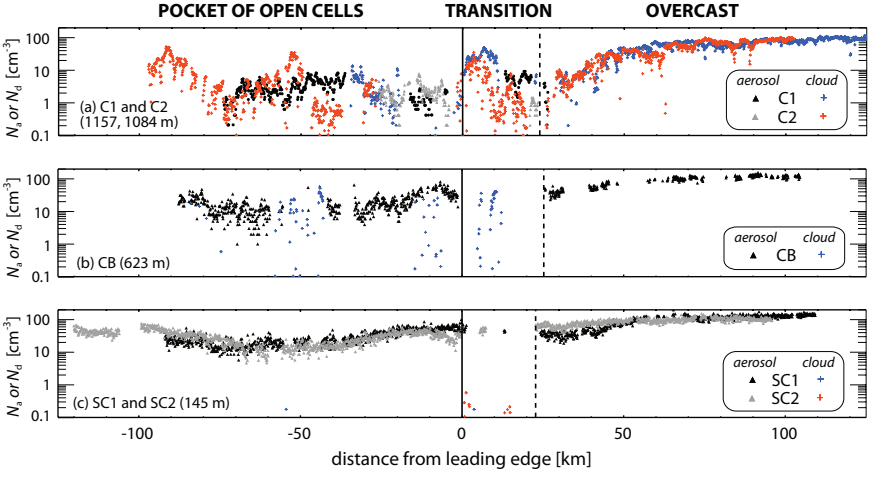

Fig. 18. Cloud droplet concentration from RF06 from the CDP N_d (colored crosses, samples in cloud) or PCASP aerosol concentration N_a (black or gray triangles, clear air samples) for **(a)** cloud layer legs C1 and C2; **(b)** cloud-base level leg CB; **(c)** subcloud legs SC1 and SC2. The data are plotted each second as a function of the distance from the leading edge of the transition region (positive towards the overcast region). Each 1 Hz data point is classified as either cloudy or clear using the criteria described in Sect. 2.4. Drizzle-containing points are excluded from the analysis since the aerosol measurement is prone to shattering artifacts.

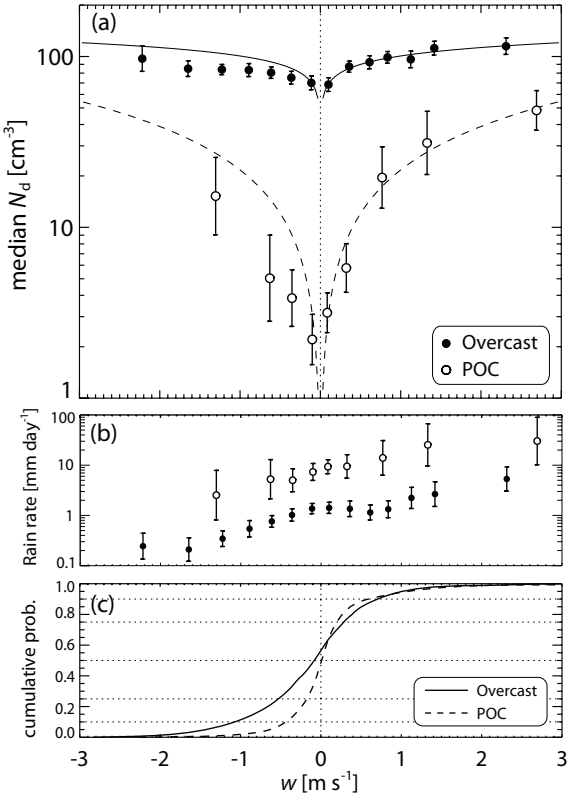

Fig. 19. (a) Median droplet concentration N_d for RF06 cloudy samples (see Sect. 2.4) binned as a function of the sample's vertical wind w magnitude in the overcast (solid circles) and POC (open circles) regions. Error bars show the approximate 95% confidence interval for the medians with degrees of freedom estimated using the approximately exponential decay of the autocorrelation function. Panel **(b)**: rain rate from the 2-D-C probe for cloudy samples binned as a function of w as in (a). Panel **(c)**: cumulative distribution function of the vertical wind from the cloud data in the overcast and POC regions.

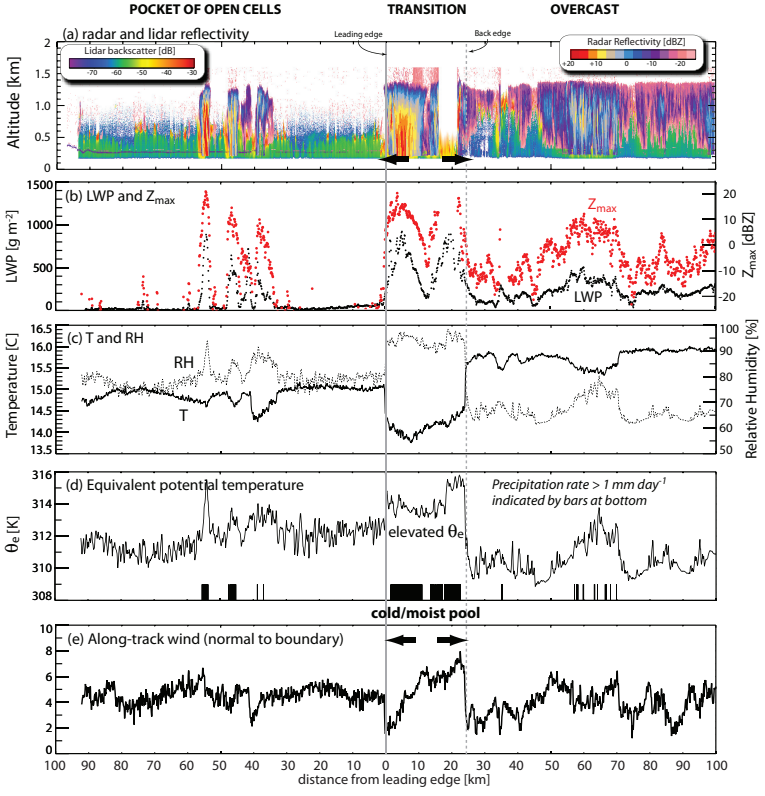

Fig. 20. **(a)** Radar and lidar aerosol reflectivity (lidar backscatter with estimated molecular backscatter subtracted and shown only where radar reflectivity below -20 dBZ); **(b)** microwave liquid water path; **(c)** temperature and relative humidity; **(d)** equivalent potential temperature and aircraft-level precipitation detection (>1 mm d^{-1} from the 2DC); **(e)** along-track (boundary-normal) wind speed for subcloud leg SC1 on RF06 showing a strong cold/moist pool with low level outflow associated with a precipitating boundary cell.

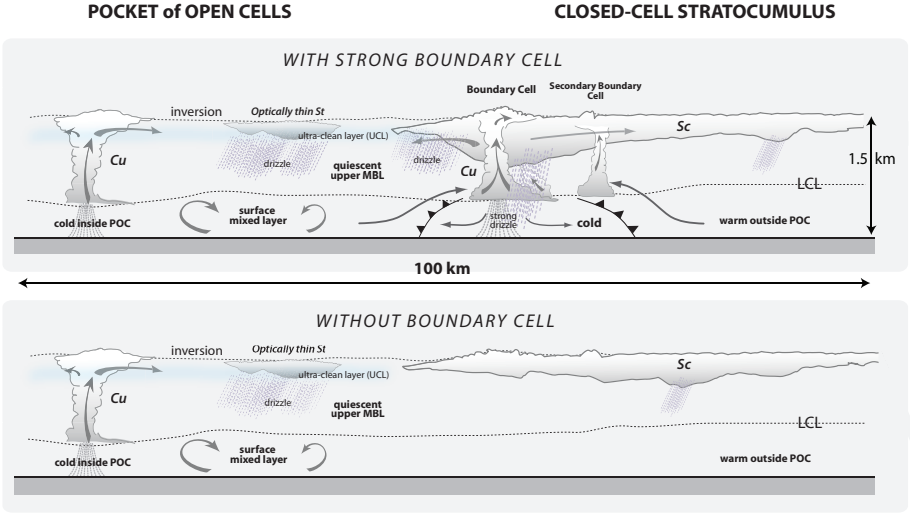

Fig. 21. Conceptual diagram of the POC-transition-overcast MBL as observed during RF06. Two realizations are shown: one in which a strong boundary cell is present, and one where no clear boundary cell is evident.

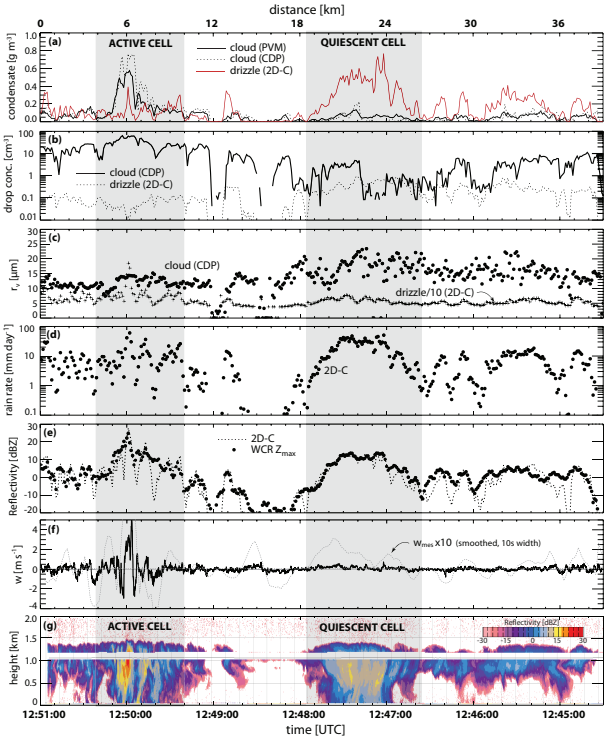

Fig. 22. Time series for 6.5 min (∼40 km) from leg C2 of RF06 at an altitude of 1084 m contrasting two cells producing strong drizzle. The panels show: **(a)** Condensed water content for cloud water (both from the PVM and the CDP) and drizzle (2-D-C); **(b)** cloud droplet and drizzle droplet concentration; **(c)** mean volume radius for cloud (CDP) and drizzle (2-D-C), note that value for drizzle is divided by 10 to facilitate use of same ordinate; **(d)** precipitation rate from the 2-D-C; **(e)** column maximum radar reflectivity $Z_{\max}$ from the WCR, and in-situ derived radar reflectivity from the 2-D-C; **(f)** vertical wind component (solid, 25 Hz) and "mesoscale" vertical wind w_{mes} smoothed with a 10 s boxcar filter (dotted) and magnified by a factor of 10; **(g)** radar reflectivity cross section from the WCR. The gray regions indicate the approximate locations of an active (left) and a quiescent (right) cell (see text).

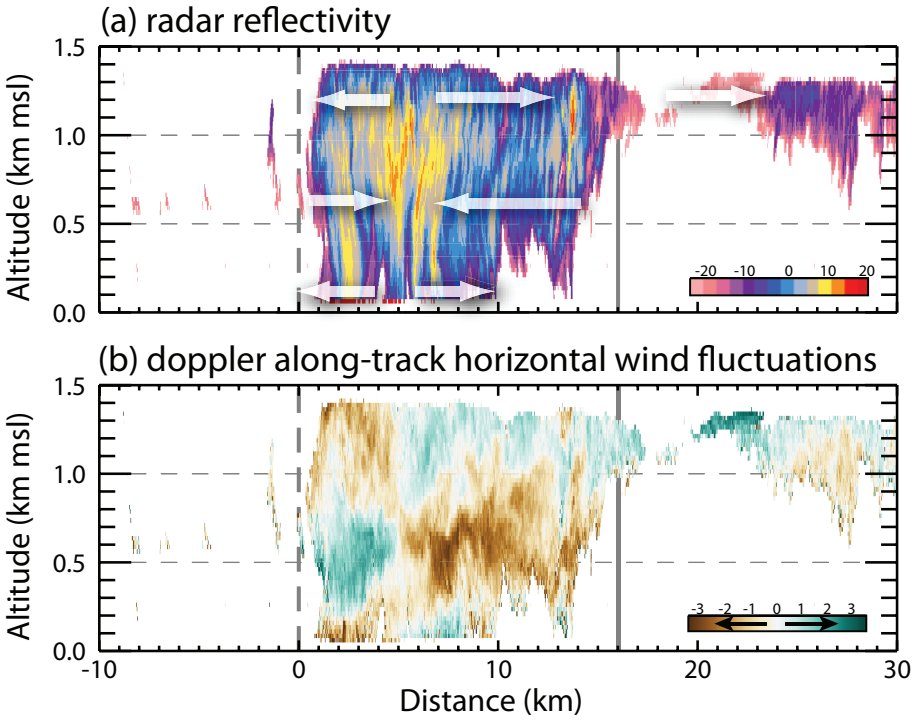

Fig. 23. **(a)** Radar reflectivity and **(b)** along-track horizontal wind component fluctuations derived from the WCR downward and slant-downward doppler (with the flight-averaged mean wind subtracted) for the AC leg during RF06.